Molecular Psychiatry
https://doi.org/10.1038/s41380-018-0308-x

ARTICLE

Ankyrin-G regulates forebrain connectivity and network synchronization via interaction with GABARAP

A. D. Nelson[1] · R. N. Caballero-Florán[1] · J. C. Rodríguez Díaz[2] · J. M. Hull[1,2] · Y. Yuan[1] · J. Li[3] · K. Chen[3] · K. K. Walder[4] · L. F. Lopez-Santiago[1] · V. Bennett[4,5] · M. G. McInnis[6] · L. L. Isom[1,2,7,8] · C. Wang[3,9] · M. Zhang[3] · K. S. Jones[1,2] · P. M. Jenkins[1,6]

Received: 11 May 2018 / Revised: 17 August 2018 / Accepted: 19 November 2018

Abstract

GABAergic circuits are critical for the synchronization and higher order function of brain networks. Defects in this circuitry are linked to neuropsychiatric diseases, including bipolar disorder, schizophrenia, and autism. Work in cultured neurons has shown that ankyrin-G plays a key role in the regulation of GABAergic synapses on the axon initial segment and somatodendritic domain of pyramidal neurons, where it interacts directly with the $GABA_A$ receptor-associated protein (GABARAP) to stabilize cell surface $GABA_A$ receptors. Here, we generated a knock-in mouse model expressing a mutation that abolishes the ankyrin-G/GABARAP interaction (*Ank3* W1989R) to understand how ankyrin-G and GABARAP regulate GABAergic circuitry in vivo. We found that *Ank3* W1989R mice exhibit a striking reduction in forebrain GABAergic synapses resulting in pyramidal cell hyperexcitability and disruptions in network synchronization. In addition, we identified changes in pyramidal cell dendritic spines and axon initial segments consistent with compensation for hyperexcitability. Finally, we identified the *ANK3* W1989R variant in a family with bipolar disorder, suggesting a potential role of this variant in disease. Our results highlight the importance of ankyrin-G in regulating forebrain circuitry and provide novel insights into how *ANK3* loss-of-function variants may contribute to human disease.

Introduction

GABAergic interneurons are essential for the proper synchronization and function of neuronal networks that underlie normal cognition, mood, and behavior. GABAergic interneurons target to unique postsynaptic domains on excitatory neurons; however, the molecular mechanisms underlying the subcellular organization of forebrain GABAergic synapses remain poorly understood. Abnormalities in GABAergic interneuron circuitry and decreased gamma oscillations have been implicated in many neurodevelopmental and neuropsychiatric disorders [1–8]. Thus, the understanding of the cellular and molecular mechanisms that contribute to the development and function of GABAergic synapses, as well as identification of genetic

Electronic supplementary material The online version of this article (https://doi.org/10.1038/s41380-018-0308-x) contains supplementary material, which is available to authorized users.

✉ P. M. Jenkins
pjenkins@umich.edu

[1] Department of Pharmacology, University of Michigan Medical School, Ann Arbor, MI 48109, USA

[2] Neuroscience Graduate Program, University of Michigan, Ann Arbor, MI 48109, USA

[3] Division of Life Sciences, State Key Laboratory of Molecular Neuroscience, Hong Kong, University of Science and Technology, Clear Water Bay, Kowloon, Hong Kong, China

[4] Department of Cell Biology, Duke University Medical Center, Durham, NC 27710, USA

[5] Departments of Biochemistry, Neurobiology, and Howard Hughes Medical Institute, Duke University Medical Center, Durham, NC 27710, USA

[6] Department of Psychiatry, University of Michigan, Ann Arbor, MI 48109, USA

[7] Department of Neurology, University of Michigan, Ann Arbor, MI 48109, USA

[8] Department of Molecular and Integrative Physiology, University of Michigan, Ann Arbor, MI 48109, USA

[9] Hefei National Laboratory for Physical Sciences at the Microscale, School of Life Sciences, University of Science and Technology of China, Hefei, China

Published online: 30 November 2018

variants that contribute to neuropsychiatric disorders is critical to the discovery of new therapeutic agents for the treatment of diseases involving altered inhibitory circuits.

ANK3 encodes ankyrin-G, a fundamental scaffolding protein that organizes critical plasma membrane domains [9, 10]. Alternative splicing of *ANK3* in the brain gives rise to three main isoforms of ankyrin-G: the canonical 190 kDa isoform, a 270 kDa isoform, and a giant, 480 kDa isoform. The 190 kDa isoform is expressed in most tissues and cell types throughout the body including brain, heart, skeletal muscle, kidney, and retina. The 270 and 480 kDa isoforms of ankyrin-G are predominantly expressed in the nervous system, and arise from alternative splicing of a single 7.8 kb giant exon [9, 11]. The 480 kDa ankyrin-G isoform has been identified as the master organizer of axon initial segments (AIS) and nodes of Ranvier, sites of action potential (AP) initiation, and propagation [10]. This splice variant is necessary for the proper clustering of voltage-gated sodium channels, KCNQ2/3 potassium channels, the cell adhesion molecule neurofascin-186, and the cytoskeletal protein βIV-spectrin to excitable domains (reviewed in ref. [12]).

Importantly, the 480 kDa ankyrin-G isoform has also been shown to stabilize GABAergic synapses on the soma and AIS of excitatory pyramidal neurons by interacting with the $GABA_A$ receptor-associated protein (GABARAP) to inhibit $GABA_A$ receptor endocytosis [13]. GABARAP and GABARAP-like 1, members of the ubiquitin-like LC3 family of microtubule-associated proteins, mediate $GABA_A$ receptor trafficking between the cell surface and intracellular compartments [14]. GABARAP and other members of the LC3 family interact with LC3-interacting region (LIR) motifs [15]. The giant exon that encodes the 480 kDa ankyrin-G isoform contains an LIR motif, which includes residue W1989 [13, 16]. Mutation of W1989 to arginine (W1989R) completely abolished the binding between ankyrin-G and GABARAP [13]. Deletion of wild-type (WT) ankyrin-G and replacement with W1989R 480 kDa ankyrin-G failed to rescue $GABA_A$ receptors to the soma and AIS or restore miniature inhibitory postsynaptic currents (mIPSCs) in cultured mouse hippocampal neurons [13]. Taken together, these findings suggested that 480 kDa ankyrin-G plays a critical role in stabilizing GABAergic synapses in vitro; however, whether ankyrin-G loss-of-function at GABAergic synapses disrupts forebrain circuitry in vivo has not been investigated.

Here, we have generated a novel knock-in mouse model expressing *Ank3* W1989R. This allowed us to study, for the first time, the relationship between the 480 kDa ankyrin-G isoform and GABAergic synapse formation and function in vivo in a model that survives to adulthood and is capable of forming the AIS and nodes of Ranvier. We show that the *Ank3* W1989R mutation causes decreases in GABAergic synapses in layer II/III of somatosensory cortex and CA1 of hippocampus, while sparing inhibitory synapses on cerebellar Purkinje neurons and thalamic neurons. The decreases in inhibitory synapses cause hyperexcitability of cortical and hippocampal pyramidal neurons and decreases in gamma oscillations. Interestingly, we also detect changes consistent with compensation for the loss of inhibitory tone, including shortening of the AIS and decreases in dendritic spine density and excitatory post synaptic currents. Finally, we report the identification of a family with bipolar disorder (BD) that carries the *Ank3* W1989R human variant (rs372922084, c.5965T > C (p.Trp1989Arg)), which may contribute to the pathophysiology of psychiatric disease.

Results

Ank3 W1989, located within the giant exon of ankyrin-G, is necessary for binding to a hydrophobic pocket in GABARAP

The 480 kDa *Ank3* splice variant interacts with GABARAP to inhibit $GABA_A$ receptor endocytosis and stabilize GABAergic synapses [13]. Here, we explored the molecular basis governing this interaction by resolving the crystal structure of the ankyrin-G/GABARAP complex. Crystallography data show that the LIR motif within the giant exon of ankyrin-G contains aromatic residues, W1989 and F1992, which insert into two hydrophobic pockets of GABARAP (Fig. 1a and Supplementary Fig. 1a). Moreover, a unique C-terminal helix extension contributes to ankyrin-G/GABARAP binding by forming a critical salt bridge between residues E1996 of ankyrin-G and R67 of GABARAP and additional hydrophobic interactions with a hydrophobic surface of GABARAP (Supplementary Fig. 1a). This newly defined binding mode with the presence of the C-terminal helix is unique compared to previously known GABARAP/LIR motifs or other LC3 family members/LIR interactions (Fig. 1b) [17], suggesting a specific neuronal function of the ankyrin-G/GABARAP interaction outside the autophagic processes for GABARAP [18]. To address the role of the W1989 residue in more detail, we performed isothermal titration calorimetry (ITC) to quantitatively measure the dissociation constant (K_d) between a series of ankyrin-G truncations and GABARAP. Using this approach, we mapped the minimal region of ankyrin-G that is capable of binding to GABARAP to a fragment of 26 amino acids (residues 1985–2010), which included residue W1989 contained within the canonical LIR motif (Supplementary Fig. 1b). This ankyrin-G fragment associated with GABARAP with a K_d of 2.9 nM, which is more than 1000-fold stronger than previously reported interactions between GABARAP and other LIR motifs (Supplementary Fig. 1c and Fig. 1b) [18]. Mutation of the W1989 residue to R abolished the interaction between

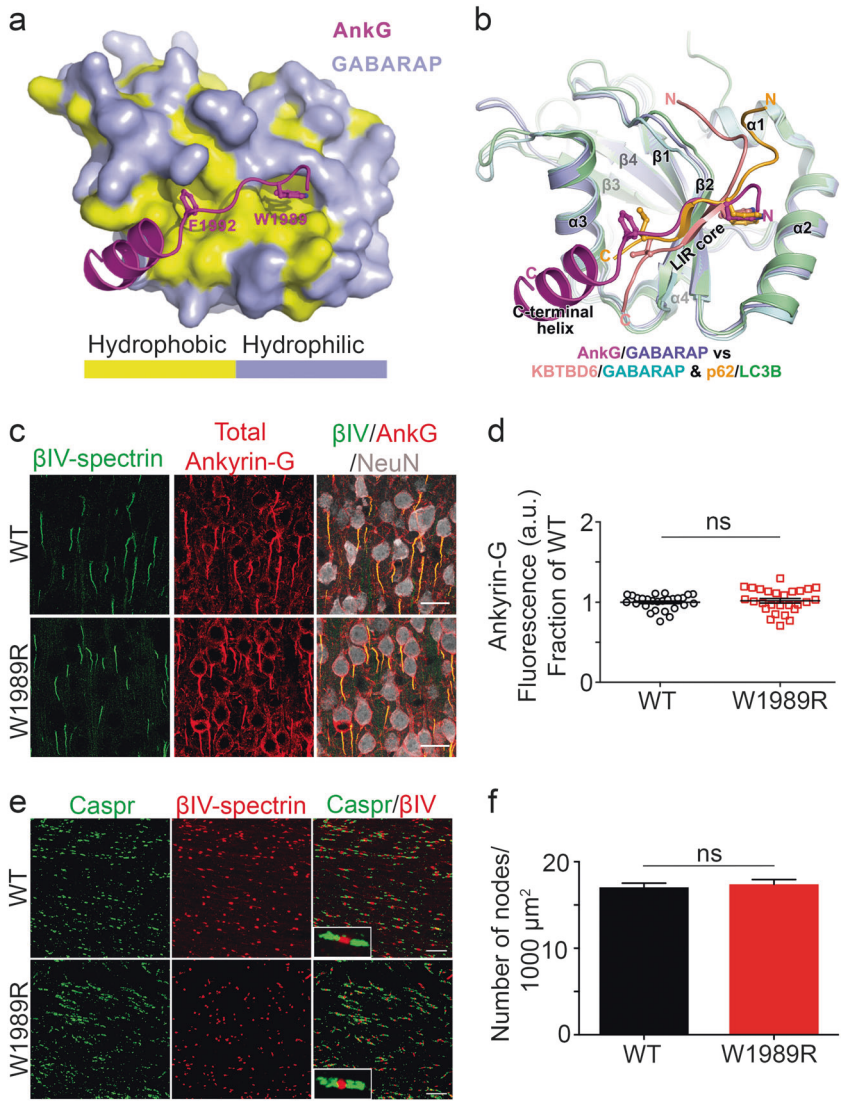

Fig. 1 AIS and nodes of Ranvier are maintained in the *Ank3* W1989R mouse model. **a** Combined surface (GABARAP) and ribbon-stick model (ankyrin-G) showing a hydrophobic pocket of GABARAP is accommodated by the critical W1989 reside within the giant exon of ankyrin-G. The surface for hydrophobic residues of GABARAP are shown in yellow while the hydrophilic surfaces are light purple. The crystal structure of ankyrin-G/GABARAP complex is at a 2.2 Å resolution. **b** Ribbon-stick model of superposition of ankyrin-G/GABARAP, KBTBD6/GABARAP, and p62/LC3B complex structures showing the comparison of ankyrin-G/GABARAP complex with common binding mode of LIR/Atg8s. **c** Representative images from coronal sections of layer II/III somatosensory cortex of P30-35 WT (top) and *Ank3* W1989R homozygous (bottom) mice. Immunostaining for βIV-spectrin (green), total ankyrin-G (red), and NeuN (white). Scale bar: 20 μm. **d** Quantification of ankyrin-G fluorescence intensity (a.u.) as fraction of WT between WT (black circles) and *Ank3* W1989R homozygous (red squares) mice. *t*-test $P = 0.5618$ (WT: 1 ± 0.02, $N = 3$, $n = 27$; W1989R: 1.02 ± 0.03, $N = 3$, $n = 27$). **e** Representative images of nodes of Ranvier from corpus callosum of P30 WT (top) and *Ank3* W1989R homozygous (bottom) mice. Sections immunostained for the paranodal marker Caspr (green) and βIV-spectrin (red). Scale bar: 20 μm. **f** Quantification of the total number of nodes of Ranvier per 1000 μm^2 from WT (black bar) and *Ank3* W1989R homozygous (red bar) mice. *t*-test $P = 0.62$, ns: not significant (WT: 17.04 ± 0.5, $N = 3$, $n = 20$; W1989R: 17.4 ± 0.5, $N = 3$, $n = 18$). Data shown as mean ± SEM

ankyrin-G and GABARAP, and decreased the binding affinity to ~11 μM, which is 4000-fold weaker than WT ankyrin-G (Supplementary Fig. 1c) [13]. Overall, these results demonstrate that ankyrin-G residue W1989 is necessary for high affinity binding to GABARAP, while F1992 and the C-terminal helix extension play important roles in maintaining this interaction.

W1989R 480 kDa ankyrin-G maintains WT functionality in assembly of the AIS and nodes of Ranvier in vivo

Several mouse models have been generated to evaluate the neuronal role of ankyrin-G in vivo; however, these mice either die early in development or lack AISs,

nodes of Ranvier, and GABAergic synapses simultaneously, making it difficult to understand the specific role of ankyrin-G-dependent GABAergic circuits [13, 16, 19]. To examine the role of 480 kDa ankyrin-G specifically in GABAergic synapse formation and function in vivo, we generated a knock-in mouse model expressing the *Ank3* W1989R ((c.5965T>C (p.Trp1989Arg)) mutation within the giant exon of ankyrin-G. Homozygous *Ank3* W1989R mice survive well into adulthood, similar to WT littermate controls, as ~90% (32/36) of *Ank3* W1989R mice live to P250 or longer. Homozygous *Ank3* W1989R mice are similar to WT mice in appearance and grooming behavior, and have no obvious neurological phenotype.

Previous studies demonstrated that expression of the W1989R 480 kDa ankyrin-G in an *Ank3* null background failed to restore $GABA_A$ receptor clustering and mIPSCs in cultured hippocampal neurons [13]. However, the W1989R mutant ankyrin-G appropriately localized to the AIS and clustered all known binding partners [13]. Thus, we expected the knock-in *Ank3* W1989R mutation to function similar to WT at the AIS and nodes of Ranvier in vivo. As predicted, immunolabeling of cortical neurons in layer II/III of the somatosensory cortex in coronal brain sections from P30 to 35 mice with antibodies specific to ankyrin-G revealed that W1989R 480 kDa ankyrin-G appropriately localized to the AIS (Fig. 1c, d). In addition, W1989R 480 kDa ankyrin-G clustered all tested ankyrin-G-binding partners to the AIS, including βIV-spectrin, neurofascin, KCNQ2 channels, and voltage-gated sodium channels (Fig. 1c and Supplementary Fig. 2).

In addition to regulating the AIS, 480 kDa ankyrin-G plays a central role in the formation and maintenance of nodes of Ranvier [16]. Analysis of the corpus callosum in homozygous *Ank3* W1989R mice revealed no detectable changes in the total number of nodes of Ranvier (Fig. 1e and f) or nodal length (WT: 1.48 ± 0.04 µm, $N = 3$, $n = 109$; W1989R: 1.6 ± 0.03 µm, $N = 3$, $n = 116$) compared to WT mice (Fig. 1f). Thus, W1989R 480 kDa ankyrin-G maintains WT functionality in forming the AIS and nodes of Ranvier in vivo.

GABAergic synapses and synaptic activity are decreased in *Ank3* W1989R forebrain pyramidal neurons in vivo

GABAergic interneurons synapse onto the dendrites, soma, and AIS of pyramidal neurons, and regulate excitability, synaptic transmission, and the synchronization of neuronal ensembles [20, 21]. To determine the effect of *Ank3* W1989R on GABAergic synapses in vivo, we immunostained WT and homozygous mutant P30-35 coronal brain sections with antibodies to the presynaptic inhibitory marker, vesicular GABA transporter (vGAT). *Ank3* W1989R mice showed a ~50–65% reduction in the number of GABAergic synapse clusters on the somatodendritic domain and AIS of cortical pyramidal neurons compared to WT neurons (Fig. 2a–c). Moreover, clustering of postsynaptic $GABA_A$ receptors was significantly decreased in dissociated hippocampal neurons from *Ank3* W1989R mice versus WT (Supplementary Fig. 3a and b). These findings demonstrate that both presynaptic and postsynaptic structural components of GABAergic synapses are lost when 480 kDa ankyrin-G is unable to interact with GABARAP in vivo.

To evaluate the functional consequences of *Ank3* W1989R on GABAergic signaling, we performed whole-cell patch-clamp recordings in acute brain slices of P25–48 WT and homozygous mutant mice. The frequency and amplitude of spontaneous inhibitory postsynaptic currents (sIPSCs) were significantly reduced in layer II/III cortical neurons, as well as CA1 hippocampal neurons of *Ank3* W1989R mice relative to WT (Fig. 2d–f and Supplementary Fig. 3c–g). The magnitude of reduction in sIPSC frequency (~65%) and amplitude (~40%) were similar between pyramidal neurons in cortical layer II/III and CA1 hippocampal neurons in *Ank3* W1989R mice compared to WT, suggesting that the binding of 480 kDa ankyrin-G to GABARAP may be a common mechanism for stabilizing GABAergic synapses in the forebrain. To address whether the decrease in quantal GABA release observed in *Ank3* W1989R mice is independent of AP firing, we measured mIPSCs in the presence of 1 µM tetrodotoxin (TTX) in acute brain slices of P25–48 mice. Consistent with the sIPSC data, we observed a significant reduction in both the frequency and amplitude of mIPSCs in *Ank3* W1989R cortical neurons versus WT (Supplementary Fig. 4a-d). The IPSC response was completely attenuated following the administration of the $GABA_A$ receptor antagonist bicuculline, confirming that the loss of inhibitory tone in *Ank3* W1989R neurons is specific to $GABA_A$ receptor function rather than by other means of inhibitory synaptic transmission (Supplementary Fig. 4d).

To determine whether the 480 kDa ankyrin-G interaction with GABARAP is specific to stabilizing forebrain GABAergic synapses, we immunostained Purkinje neurons in the cerebellum and thalamic neurons of P30–35 mice with antibodies against vGAT. We found that W1989R 480 kDa ankyrin-G is capable of stabilizing pinceau synapses at the AIS, as well as somatodendritic GABA synapses on cerebellar Purkinje neurons (Supplementary Fig. 5a–c). The frequency and amplitude of sIPSCs and mIPSCs of Purkinje neurons were unchanged in *Ank3* W1989R mice relative to WT (Supplementary Fig. 5d–h). In addition, we found no difference in the number of vGAT-positive puncta on the soma or AIS of thalamic neurons in *Ank3* W1989R mice as compared to WT (Supplementary Fig. 6a–c). The function

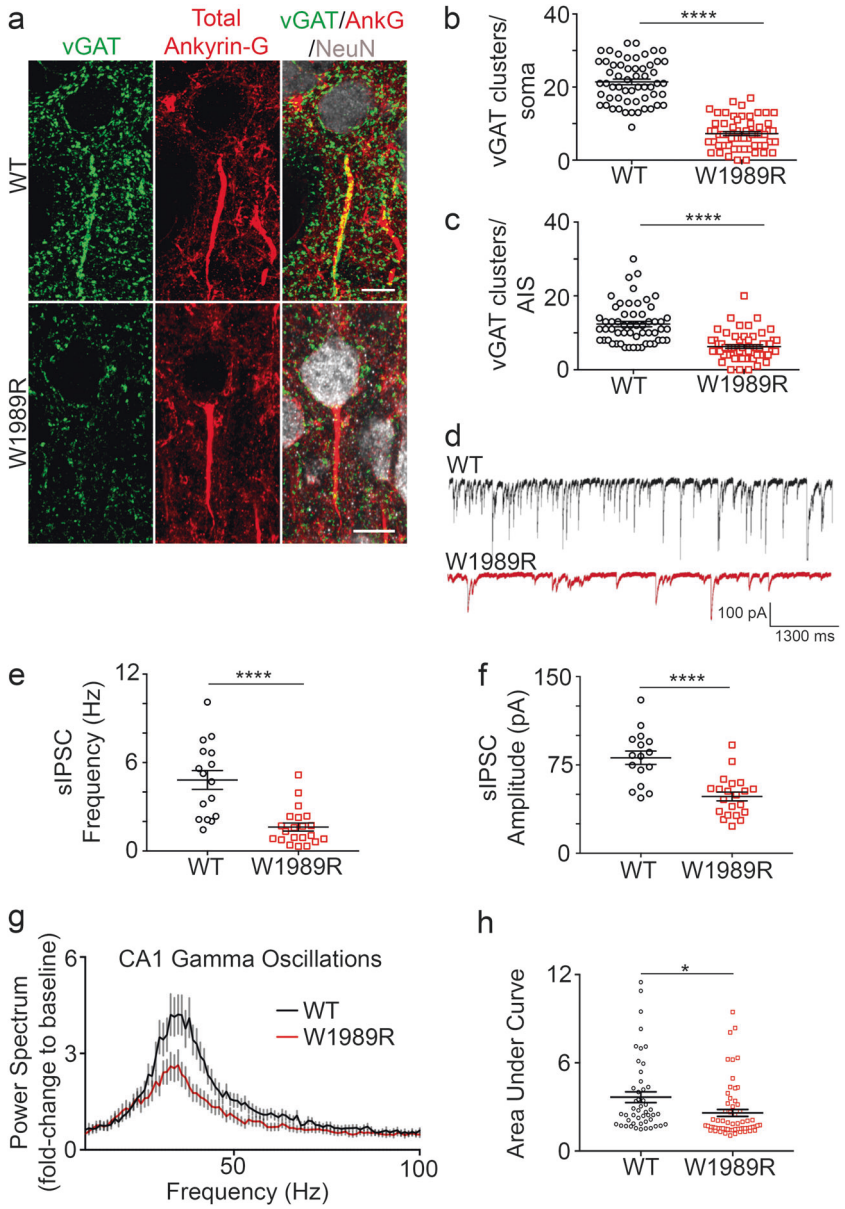

Fig. 2 GABAergic synapses are reduced in *Ank3* W1989R mice resulting in decreased gamma oscillations. **a** Representative images of GABAergic synapses from layer II/III somatosensory cortex of P25-48 WT (top) and *Ank3* W1989R homozygous (bottom) mice. Coronal brain sections immunostained with a presynaptic GABAergic marker vGAT (green), total ankyrin-G (red), and NeuN (white). Scale bar: 20 µm. **b** Quantification of the total number of vGAT-positive clusters per soma above a set intensity threshold from WT (black circles) and *Ank3* W1989R homozygous (red squares) mice. *t*-test $^{****}P < 0.0001$ (WT: 21.42 ± 0.8, $N = 3$, $n = 57$; W1989R: 7.25 ± 0.5, $N = 3$, $n = 60$). **c** Quantification of total number of vGAT-positive clusters per AIS from WT (black circles) and *Ank3* W1989R homozygous (red squares) mice. *t*-test $^{****}P < 0.0001$ (WT: 12.38 ± 0.7, $N = 3$, $n = 56$; W1989R: 6.27 ± 0.5, $N = 3$, $n = 60$). **d** Spontaneous inhibitory postsynaptic current (sIPSC) representative traces from layer II/III somatosensory cortical neurons in WT (black) and *Ank3* W1989R (red) slices. Scale bars: 100 pA, 1300 ms. **e** Quantification of sIPSC frequency from layer II/III somatosensory cortical neurons in WT (black circles) and *Ank3* W1989R (red squares) brain slices. *t*-test $^{***}P < 0.0001$ (WT: 4.82 ± 0.6 Hz, $n = 16$; W1989R: 1.63 ± 0.3 Hz, $n = 21$). **f** Quantification of sIPSC amplitude from layer II/III somatosensory cortical neurons in WT (black circles) and *Ank3* W1989R (red squares) brain slices. *t*-test $^{***}P < 0.0001$ (WT: 81.1 ± 5.7 pA, $n = 16$; W1989R: 48.22 ± 3.7 pA, $n = 21$). **g** Power spectral analysis from CA1 hippocampus in acute brain slices of P24-40 WT (black circles) and *Ank3* W1989R homozygous (red squares) mice plotted as fold-change to baseline signal. **h** Quantification of the area under the curve for gamma band (30–60 Hz) from CA1 hippocampus in WT (black circles) and *Ank3* W1989R homozygous (red squares). *t*-test $^{*}P = 0.0118$ (WT: 3.66 ± 0.4, $N = 3$, $n = 48$; W1989R: 2.59 ± 0.2, $N = 3$, $n = 62$). Data shown as mean ± SEM

of GABA-mediated currents was also unchanged in *Ank3* W1989R thalamic neurons, as sIPSC and mIPSC frequency and amplitude were not significantly different than WT thalamic neurons (Supplementary Fig. 6d–h). Overall, these results demonstrate that stabilization of cell surface $GABA_A$ receptors mediated by 480 kDa ankyrin-G and GABARAP

is a cell type-specific and brain region-specific mechanism for the proper formation and function of GABAergic synapses in vivo.

Homozygous *Ank3* W1989R mice show altered network synchronization

Parvalbumin-positive (PV+) GABAergic interneurons are critical for the synchronization of forebrain networks due to their rhythmic, fast-spiking electrophysiological properties, and because a single PV+ interneuron can synapse onto hundreds or thousands of pyramidal neurons simultaneously [22, 23]. There are two main subtypes of PV+ interneurons: the PV+ basket cells, which synapse onto the soma and proximal dendrites of pyramidal neurons, and PV+ chandelier cells, which innervate the AIS. Decreased GABAergic synapses and sIPSC frequency observed in the *Ank3* W1989R mouse model (Fig. 2 and Supplementary Fig. 3) suggested a reduction in presynaptic connectivity or reduced density of PV+ interneurons. To test this hypothesis, we measured PV+ cell number and function in layer II/III of the somatosensory cortex. Immunostaining of coronal brain sections with anti-PV antibodies revealed no detectable changes in the density of PV+ interneurons in *Ank3* W1989R mice compared to WT (Supplementary Fig. 7a and b). To evaluate the firing properties of PV+ interneurons, we evoked AP firing by injecting somatic current in acute brain slices of P25–48 homozygous *Ank3* W1989R or WT mice. *Ank3* W1989R PV+ interneurons maintained their fast-spiking electrophysiological properties and demonstrated similar AP frequency and amplitude compared to WT PV+ neurons (Supplementary Fig. 7c, e, and f). We observed a significant increase in the membrane resistance in *Ank3* W1989R PV+ interneurons compared to WT (Supplementary Fig. 7d), suggesting decreased ion channel expression at the plasma membrane.

PV+ interneurons comprise ~40% of the total number of interneurons in the somatosensory cortex [24]. To examine the effect of the *Ank3* W1989R mutation on two additional subclasses of GABAergic interneurons, we performed whole-cell patch clamp recording on regular spiking non-pyramidal interneurons (RSNP) and irregular spiking interneurons (IS). Despite a large decrease in detectable GABAergic synapse connectivity, there was no significant difference in AP frequency or amplitude of RSNP interneurons or IS interneurons in *Ank3* W1989R mice compared to WT (Supplementary Table 2). Moreover, there was a significant reduction in AP threshold from RSNP and IS interneurons between WT and *Ank3* W1989R mice; however, the input resistance, resting membrane potential, AP amplitude, and AP τ were unchanged (Supplementary Table 2). These data suggest that loss-of-function of the 480 kDa isoform of ankyrin-G results in decreases in GABAergic synaptic connectivity; however, GABAergic inhibitory interneurons are present at normal density and are capable of functioning.

PV+ interneurons are responsible for the synchronization of neuronal networks, which results in the generation of gamma oscillations [23]. Gamma oscillations reflect the synchronization of local neuronal network activity providing a "temporal framework" for proper information processing, sensory integration, and cognitive function [22, 25, 26]. We hypothesized that, because *Ank3* W1989R mice exhibit reductions in somatodendritic and AIS GABAergic synapses, network synchronization would be decreased resulting in a reduction in the power of gamma oscillations. To evaluate the synchronization of neuronal ensembles, we used planar multi-electrode arrays to record kainate-induced gamma oscillations in acute slices of hippocampus from WT and homozygous *Ank3* W1989R mice [27] (Supplementary Fig. 8a and b). The power of the kainate-induced gamma oscillations was ~30% decreased in CA1 and CA3 hippocampal regions in *Ank3* W1989R mice compared to WT (Fig. 2g and h and Supplementary Fig. 8c–f). This significant reduction in gamma oscillations in *Ank3* W1989R mouse hippocampus suggests disruptions in network synchrony, consistent with reduced connectivity of PV+ interneurons.

Dendritic spine density and function are reduced in Ank3 W1989R neurons

GABAergic interneurons control the excitability of glutamatergic pyramidal neurons by modulating their spike timing and firing rate. The loss of inhibitory tone, similar to that observed here in *Ank3* W1989R mice, has been linked to pathological neuronal hyperexcitability [28]. To address the effect of decreases in GABAergic synapses on AP firing rates, we compared evoked APs in acute brain slices of P25–48 homozygous *Ank3* W1989R and WT mice. The frequency of AP firing was significantly increased in *Ank3* W1989R cortical and CA1 hippocampal neurons compared to WT (Fig. 3a, c, d, f). Moreover, the maximum firing rate per neuron was two-fold higher in *Ank3* W1989R neurons versus WT (Fig. 3b, e). These data demonstrate that cortical and hippocampal pyramidal neurons are hyperexcitable in vivo following 480 kDa ankyrin-G loss-of-function at GABAergic synapses.

Neurons have developed multiple intrinsic mechanisms to maintain excitability homeostasis and stabilize network activity. The AIS has been proposed to participate in activity-dependent plasticity and decreasing AIS length may be one mechanism to reduce excitability. We measured AIS length of layer II/III somatosensory cortical neurons in coronal brain sections in P30 mice and in dissociated hippocampal neurons at 21 DIV from WT and

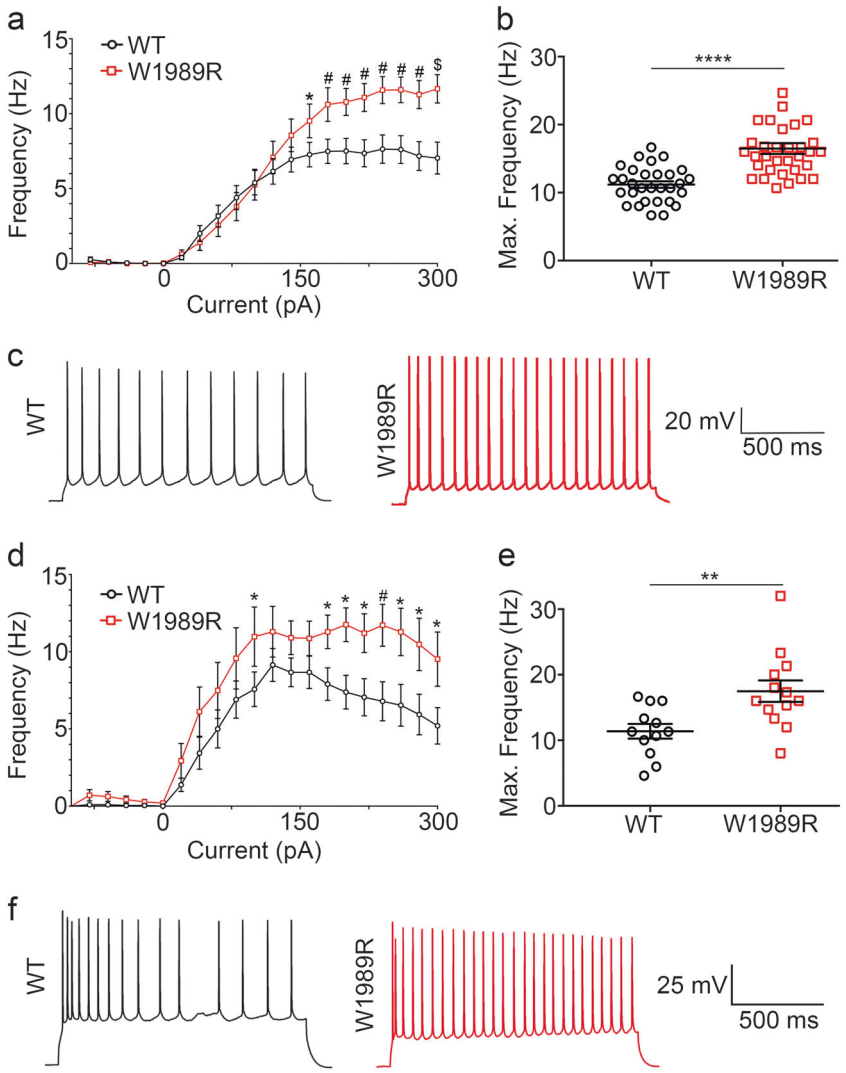

Fig. 3 Increased firing rate of *Ank3* W1989R cortical and CA1 hippocampal pyramidal neurons. **a** Evoked AP frequency from cortical neurons for WT (black circles) or *Ank3* W1989R homozygous (red squares) in acute brain slices. Two-way ANOVA, Tukey's post hoc $^{*}P < 0.05$, $^{\#}P < 0.001$, $^{\$}P < 0.001$ (WT: $n = 40$; W1989R: $n = 40$). **b** Quantification of average maximum frequency of pyramidal neurons in layer II/III somatosensory cortex in WT (black circles) and *Ank3* W1989R homozygous (red squares) mice. *t*-test $^{****}P < 0.0001$ (WT: 11.18 ± 0.5, $n = 30$; W1989R: 16.49 ± 0.8, $n = 33$). **c** Representative AP traces from cortical pyramidal neurons of WT (left, black) and *Ank3* W1989R homozygous (right, red) mice. Scale bar: 500 ms. **d** Evoked AP frequency from CA1 hippocampal neurons for WT (black circles) or *Ank3* W1989R homozygous (red squares) in acute brain slices. Two-way ANOVA, Tukey's post hoc $^{*}P < 0.05$, $^{\#}P < 0.001$ (WT: $n = 27$; W1989R: $n = 27$). **e** Quantification of average maximum frequency of pyramidal neurons in CA1 hippocampus of WT (black circles) and *Ank3* W1989R homozygous (red squares) mice. *t*-test $^{**}P = 0.0061$ (WT: 11.38 ± 1.1, $n = 12$; W1989R: 17.49 ± 1.6, $n = 13$). **f** Representative traces from CA1 hippocampal pyramidal neurons of WT (left) and *Ank3* W1989R homozygous (right) mice. Scale bar: 500 ms. Data shown as mean ± SEM

Ank3 W1989R mutant mice. We found that AIS length was ~30% shorter in *Ank3* W1989R mice compared to WT (Supplementary Fig. 9). Consistent with no change in inhibitory tone (Supplementary Figs. 5 and 6), there was no detectable difference in AIS length of cerebellar Purkinje neurons (WT: 15.3 ± 1.2 µm, $N = 3$, $n = 12$; W1989R: 14.9 ± 0.6 µm, $N = 3$, $n = 14$ *t*-test $P = 0.72$) or thalamic neurons (WT: 21.8 ± 0.7 µm, $N = 3$, $n = 34$; W1989R: 21.6 ± 0.9 µm, $N = 3$, $n = 29$ *t*-test $P = 0.88$) in *Ank3* W1989R mice compared to WT mice.

Another neuronal mechanism to compensate for the lack of inhibitory tone is to decrease AMPA receptor surface expression and decrease dendritic spine density [29]. We therefore examined dendritic spine density in dissociated hippocampal neurons and CA1 hippocampal neurons in vivo from *Ank3* W1989R mice and observed a significant decrease in the total number of dendritic spines compared to WT (Fig. 4a, b and Supplementary Fig. 10a and b). Consistent with this result, whole-cell patch clamp recordings from CA1 hippocampal neurons in brain slices

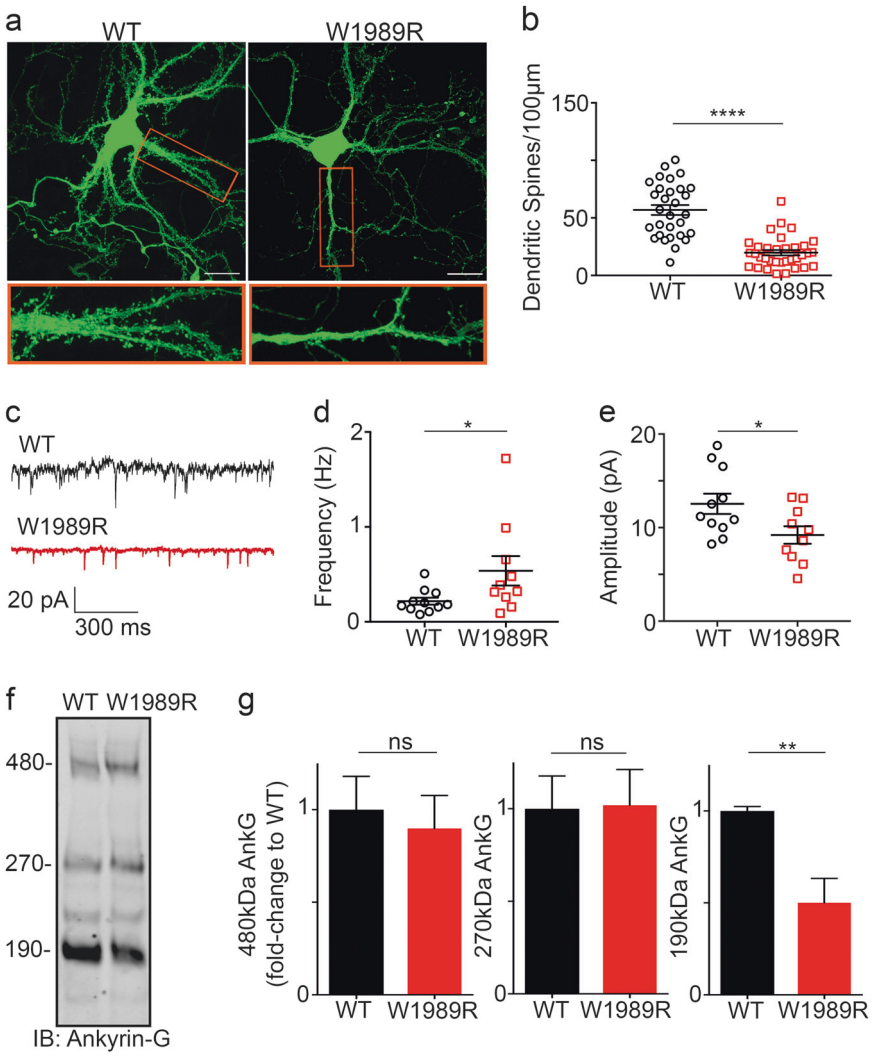

Fig. 4 Decreased spine density and function and reduced 190 kDa ankyrin-G expression levels in *Ank3* W1989R neurons. **a** Representative images of dissociated hippocampal cultured neurons from WT (left) and *Ank3* W1989R homozygous (right) mice at 21DIV filled with soluble eGFP. Scale bar: 20 µm. **b** Quantification of the total number of dendritic spines per 100 µm per neuron. *t*-test ****$P <$ 0.0001 (WT: 56.91 ± 4.3, $N = 3$, $n = 30$; W1989R: 19.78 ± 2.3, $N = 3$, $n = 34$). **c** Representative traces of spontaneous excitatory postsynaptic currents (sEPSCs) from CA1 hippocampal neurons in WT (top) and *Ank3* W1989R (bottom) slices. Scale bar: 300 ms. **d** Quantification of mEPSC frequency in WT (black circles) and *Ank3* W1989R (red squares) brain slices. *t*-test *$P = 0.049$ (WT: 0.22 ± 0.04 Hz, $n = 11$; W1989R: 0.54 ± 0.15 Hz, $n = 10$). **e** Quantification of mEPSC amplitude in WT (black circles) and *Ank3* W1989R (red squares) brain slices. *t*-test *$P = 0.032$ (WT: 12.5 ± 1.1 pA, $n = 11$; W1989R: 9.21 ± 0.9 pA, $n = 10$). **f** Western blot analysis from hippocampal lysates of P30 WT (left) and *Ank3* W1989R homozygous (right) mice. Blots were probed with antibodies to total ankyrin-G. Quantification of relative expression levels of 480 kDa ankyrin-G *t*-test $P = 0.71$ (WT: 1.0 ± 0.2, $N = 3$; W1989R: 0.9 ± 0.2, $N = 3$), 270 kDa ankyrin-G *t*-test $P = 0.95$ (WT: 1.0 ± 0.2, $N = 3$; W1989R: 1.019 ± 0.2, $N = 3$), and 190 kDa ankyrin-G *t*-test *$P = 0.02$ (WT: 1 ± 0.02 $n = 3$; W1989R: 0.5 ± 0.1, $N = 3$). Data normalized to WT controls. Data shown as mean ± SEM

showed significant decreases in miniature excitatory postsynaptic current (mEPSC) amplitude in *Ank3* W1989R mice compared to WT, suggesting a reduction in dendritic AMPARs (Fig. 4c, e). Moreover, mEPSC frequency was increased in *Ank3* W1989R neurons (Fig. 4d). A previous study showed that 190 kDa ankyrin-G plays a critical role in modulation of dendritic spine morphology and AMPA receptor postsynaptic stability [30]. Western blot analysis of hippocampal and cortical lysates from *Ank3* W1989R mice showed a 50% decrease in 190 kDa ankyrin-G expression, with no change in the expression of the 270 or 480 kDa splice variants, compared to WT lysates (Fig. 4f and Supplementary Fig. 11). Overall, these data suggest a novel intrinsic mechanism to compensate for neuronal hyperexcitability by decreasing the expression of 190 kDa ankyrin-G and subsequently dendritic spine density and function in neurons with reduced inhibitory tone.

Identification of *ANK3* W1989R in a family with BD

Disruptions in forebrain circuitry and network-level activity observed in *Ank3* W1989R mice predict that patients expressing this variant may experience altered brain activity and mood-related behaviors. According to the most recent data from the gnomAD project, the *ANK3* W1989R variant (rs372922084, c.5965T>C (p.Trp1989Arg)) is found in approximately 1:10,000 European Americans [31]. We used whole genome and exome sequencing on blood samples from ~600 BD patients obtained through the Heinz C. Prechter Bipolar Research Program at the University of Michigan to identify a patient expressing the *ANK3* W1989R variant (Fig. 5a). We confirmed the presence of the variant by extracting DNA from fibroblasts derived from the proband and performing nested PCR followed by Sanger sequencing. The proband (II:2, age 45) was diagnosed with BD type I characterized by recurrent mania and depression with an age of onset of 17 years, and was successfully maintained on lithium (1200 mg daily) and a benzodiazepine (pro re nata) PRN at bedtime. The proband had a brief (<3 months) exposure to antipsychotic medication (chlorpromazine), but no history of treatment with antidepressant medication. To determine whether other family members also carried the *ANK3* W1989R variant, we expanded our studies to include the proband's parents (I:1, I:2) and sister (II:1). We extracted DNA from whole blood and performed nested PCR of the region flanking *ANK3* W1989 followed by Sanger sequencing. The proband (II:2), the mother (I:2), and the sister (II:1) were heterozygous for the *ANK3* W1989R variant (Fig. 5a, b). The mother (age 73) was diagnosed with BD type I with age of onset in her mid-

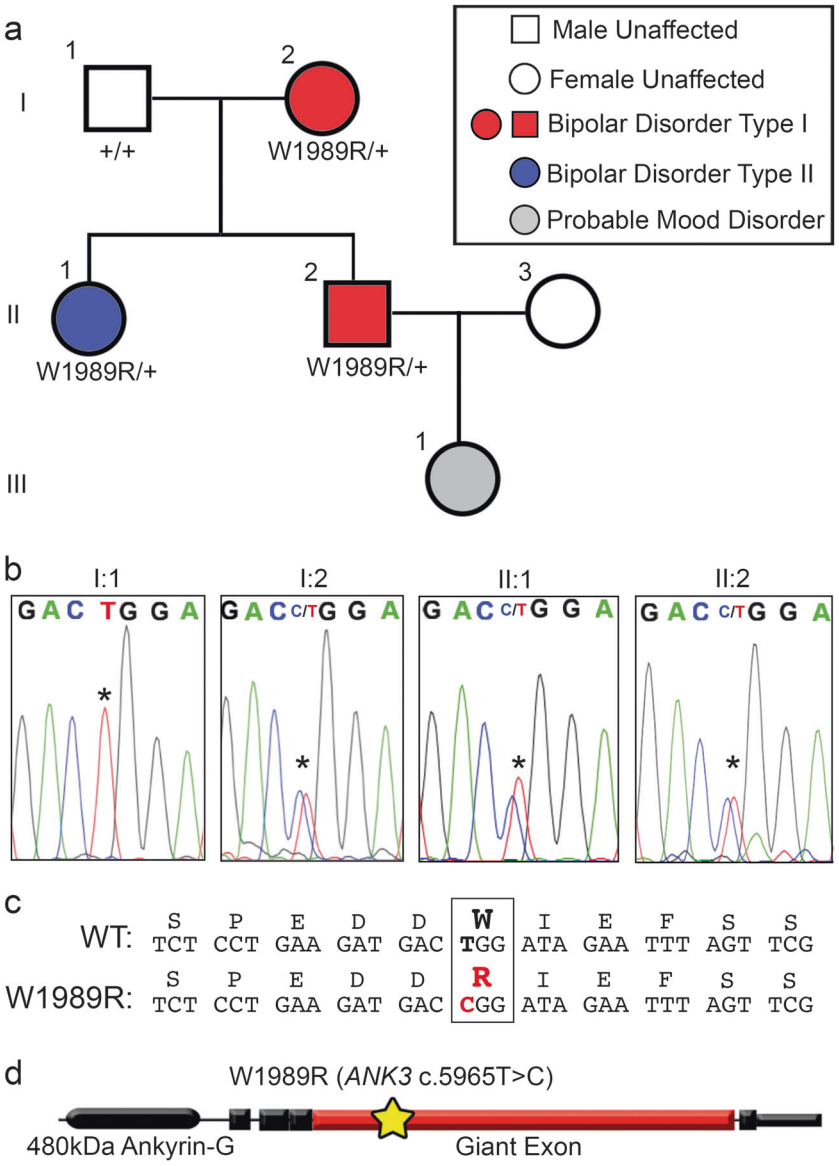

Fig. 5 *ANK3* W1989R variant identified in a family with bipolar disorder. **a** Pedigree of individuals heterozygous for *ANK3* W1989R mutation diagnosed with BD. Red: diagnosis of BD type I. Blue diagnosis of BD type II. Gray: individuals with signs and symptoms of mood disorders. White: neurotypical individuals. Circles: female. Squares: male. The affected proband is individual II:2 represented by a red square. **b** Chromatogram from Sanger sequencing confirming presence of *ANK3* W1989R heterozygous mutation in affected mother I:2, affected proband II:2, and proband's affected sister II:1. Asterisk: site of missense mutation in affected individuals I:2, II:1, and II:2 or wild-type allele in I:1. **c** The nucleotide sequence alignment and single-letter amino acid translation of the coding non-synonymous heterozygous W1989R mutation. The W1989R missense mutation c.5965T>C (p.Trp1989Arg) identified in the individuals with BD is highlighted in red. **d** Schematic of the 480 kDa splice variant of ankyrin-G. Yellow star: site of W1989R variant (c.5965T>C) ((p.Trp1989Arg)) within the giant exon (red) of ankyrin-G

30s. She was treated in the community with lamotrigine (50 mg daily), clomipramine (50 mg daily), and lorazepam (1–3 mg daily), as needed, for anxiety. Lamotrigine was given for mood stabilization. The proband's sister (age 50) was diagnosed with BD type II, with a prepubertal onset of mood instabilities and multiple episodes of depression and hypomania with mixed affective features. She was treated with antidepressants (fluoxetine 60 mg and buproprion 300 mg daily), an anticonvulsant (lamotrigine 400 mg daily), a stimulant (amphetamine 60 mg daily), and a hypnotic (temazepam 30 mg at bedtime). The proband's daughter (age 19) was diagnosed with major depression, but no DNA sample was available. The father (I:1) was WT for W1989 and had no history of depression or treatment of any psychiatric disorder (Fig. 5b). This is the first reported characterization of the *ANK3* W1989R human variant (c.5965T>C (p.Trp1989Arg)) (Fig. 5c). Similar to results from *Ank3* W1989R mutant mice, patients carrying the *ANK3* W1989R variant have survived into adulthood, demonstrating that this variant is compatible with normal lifespan in humans. However, the presence of the *ANK3* W1989R variant in three affected patients is consistent with a potential effect of this variant on neuronal activity and mood-related behaviors.

The individuals in the family diagnosed with BD are all heterozygous for *ANK3* W1989R variant. To test the effect of the *Ank3* W1989R variant on GABAergic circuitry in heterozygous mice, we measured sIPSCs and mIPSCs in layer II/III somatosensory cortical neurons of P30 mice. Heterozygous *Ank3* W1989R mice showed a significant reduction in sIPSC frequency (~50%) and amplitude (~40%) compared to WT mice (Supplementary Fig. 12a, b, and e). The frequency of mIPSCs was also significantly reduced in heterozygous *Ank3* W1989R compared to WT mice, with no change in mIPSC amplitude (Supplementary Fig. 12c, d, and f). These results show that the presence of a single copy of *Ank3* W1989R is sufficient to significantly impact inhibitory signaling in forebrain and suggest that the presence of this variant could contribute to the pathophysiology of BD.

Discussion

Neuropsychiatric diseases, such as BD and schizophrenia, are highly heritable. Significant progress has been made in the past decade identifying genetic risk factors associated with neuropsychiatric diseases including common single nucleotide polymorphisms (SNPs) through GWAS, copy number variants, and rare inherited and de novo variants [32]. For many neurological diseases, common genetic variants have minimal impact on disease susceptibility, thus it is important to understand how rare genetic variants impact brain function and underlie the pathophysiology of neuropsychiatric disease. *ANK3* is among the most consistent and significant genes associated with BD [33–36]; however, the mechanisms by which *ANK3* variants contribute to pathophysiology are not known. Although *ANK3* has been associated with multiple neurological disorders, the cellular and molecular mechanisms by which its loss-of-function contributes specifically to BD are poorly understood.

In this study, we generated homozygous *Ank3* W1989R knock-in mice to investigate ankyrin–G/GABARAP interactions and to understand the effects of 480 kDa ankyrin-G loss-of-function at GABAergic synapses in vivo (Table 3). We found that *Ank3* W1989R mice have reduced GABAergic synapses on the AIS and somatodendritic domain of cortical and hippocampal pyramidal neurons, while the density and function of PV+ GABAergic interneurons are maintained. Gamma oscillations were reduced in *Ank3* W1989R hippocampus, suggesting disruptions in network synchrony, consistent with reduced connectivity of PV+ interneurons. We found that AIS length and dendritic spine density and function were reduced in *Ank3* W1989R cortical and hippocampal neurons, suggesting that regulation of ankyrin-G-dependent domains may be a neuronal mechanism of homeostasis. Finally, we identified the *ANK3* W1989R variant rs372922084 (c.5965T>C (p.Trp1989Arg)) in a family with BD, suggesting that *ANK3* W1989 is a critical residue involved in disease mechanisms in human patients.

The decrease in AIS length in *Ank3* W1989R mice may be due to neural plasticity changes, as recent reports have shown that alterations in AIS length, location, and/or ion channel surface expression may occur following fluctuations in neuronal activity in an attempt to maintain homeostasis of intrinsic excitability [37]. Further, we propose that the decreased dendritic spine density and function observed in *Ank3* W1989R mice may be an additional compensatory mechanism to modulate neuronal hyperexcitability. The W1989R mutation is specific to the giant exon, only included in the 270 and 480 kDa splice variants of ankyrin-G, which suggests that the observed decrease in 190 kDa ankyrin-G expression may be a compensatory effect to maintain excitatory/inhibitory balance. It is possible that changes in expression levels of the 190 kDa ankyrin-G may be a common mechanism for modulating dendritic spine morphology and function to compensate for altered neuronal excitability. Future experiments will be necessary to understand the mechanisms by which genetic or pharmacological manipulation of neuronal excitability changes expression of 190 kDa ankyrin-G and dendritic spines. Further, the observed increase in mEPSC frequency may be explained by hyperexcitability of upstream glutamatergic neurons due to the decrease in inhibitory synapses.

Our work shows that the interaction between 480 kDa ankyrin-G and GABARAP is necessary for stabilizing forebrain GABAergic synapses, while additional mechanisms are involved in the formation of GABAergic synapses in the cerebellum and thalamus. Previous studies have shown that deletion of 480 kDa ankyrin-G in vivo results in the loss of GABAergic synapses at the AIS of cerebellar Purkinje neurons [13, 16]. Further, a study by Ango et al. showed an ankyrin-G-dependent subcellular gradient of neurofascin-186 at the AIS of Purkinje neurons is necessary for organizing GABAergic synapses [38]. These findings suggest that, while the formation of GABAergic synapses onto the AIS of cerebellar Purkinje neurons is mediated by 480 kDa ankyrin-G, this mechanism requires the clustering of neurofascin-186 and is independent of the ankyrin-G/GABARAP mechanism [38]. In addition, abolishing the interaction between 480 kDa ankyrin-G and GABARAP did not affect the number or function of thalamic neuron GABAergic synapses, suggesting the formation of thalamic inhibitory synapses is controlled by an alternative mechanism. Future studies are needed to understand the postsynaptic mechanisms underlying GABAergic synapse formation and stabilization in other brain regions. Our results demonstrate that ankyrin-G plays a critical role in stabilizing GABAergic synapses through brain region-specific and cell type-specific mechanisms.

Several mouse models have been generated to understand how *Ank3* contributes to neuronal development and function. Specific deletion of the exon encoding the giant 270 and 480 kDa isoforms of ankyrin-G results in the loss of all known AIS components, gross malformations in the morphology and total number of nodes of Ranvier, and decreased GABAergic inhibitory synapses. This genetic manipulation also results in lethality at P20, preventing the study of mature animals [16]. A recent study generated a mouse model with forebrain-specific deletion of all splice variants of ankyrin-G[39]. These ankyrin-G conditional null mice demonstrate "mania-like" behaviors including hyperactivity, decreased anxiety, and exploratory behavior, as well as depressive-like behaviors following social defeat stress [39]. The behavioral phenotypes identified in this model were rescued following administration of lithium and valproic acid [39]. Although the animals survived well into adulthood, the loss of the AIS, nodes of Ranvier, and GABAergic synapses simultaneously made it difficult to determine which ankyrin-G-dependent domain underlies the observed behavioral phenotypes related to BD. A study by Lopez et al. showed that deletion of *Ank3* exon 1b, which affects ankyrin-G splice variants encoded by alternative first exon and N-termini splicing, results in decreased ankyrin-G expression at the AIS of PV+ interneurons [40]. These investigators found that gene dosage-dependent reductions in expression of ankyrin-G corresponded to disease severity. Heterozygous mice displayed behavioral phenotypes representative of BD, whereas homozygous mice demonstrated epilepsy and sudden death [40]. In contrast to the *Ank3* W1989R mice, which display no change in the expression of 480 kDa ankyrin-G at the AIS, *Ank3* exon 1b mice show decreased expression of ankyrin-G at the AIS of PV+ interneurons. Reduced ankyrin-G expression at the AIS results in decreased inhibitory conductance due to changes in PV+ interneuron intrinsic excitability in *Ank3* exon 1b mice compared to the loss of GABAergic connectivity as seen in the *Ank3* W1989R mice. Intriguingly, despite the differences in mechanisms, both models result in reduced inhibitory tone and altered excitation/inhibition balance.

Another study compared the behaviors of *Ank3* heterozygous null mice with mice in which ankyrin-G was deleted specifically in the hippocampal dentate gyrus using short hairpin RNA (shRNA) viral vectors [41]. Both models demonstrated reduced anxiety and increased impulsivity, behavioral phenotypes related to BD [41]. These behaviors were reversed following chronic lithium treatment [41]. Taken together, these studies, along with the present work, provide evidence that *ANK3* is critical for normal brain function.

Abnormalities in excitatory/inhibitory circuit balance have been implicated in the pathophysiology of BD and schizophrenia [42–48]. Postmortem brains of BD patients revealed decreased expression of the GABAergic synapse marker GAD_{67}, the GABA transporter GAT1, and various $GABA_A$ receptor subunits [3, 4, 49]. We found morphological and functional reductions in cortical and hippocampal GABAergic synapses in the *Ank3* W1989R mouse model, consistent with GABAergic dysfunction reported in patients with BD [42]. Cortex and hippocampus are key brain regions associated with the cognitive, emotional, and mood-related behaviors characteristic of BD [1]. Further, abnormalities in dendritic spines have been associated with neuropsychiatric diseases including BD, schizophrenia, autism spectrum disorders, and intellectual disability [43, 44, 46–48]. We found reduced density and function of dendritic spines in our mouse model and proposed that these effects act to modulate hyperexcitability and compensate for the lack of inhibitory input. Previous studies have observed impairments in gamma oscillations in patients with neuropsychiatric disease, including BD and schizophrenia [2, 6–8, 28]. Further, recent reports have suggested that gamma oscillations may serve as biomarkers for diagnosing and tracking treatment response in individuals with BD [5]. Consistent with these studies, we found significant decreases in hippocampal gamma oscillations in the *Ank3* W1989R mice. A study by Ozerdema et al. showed a ~35% reduction in gamma oscillations in patients with BD, which is similar in magnitude to that seen in our mouse model, suggesting that even modest defects in network synchronization can have significant clinical effects [50]. Thus, our

cellular and functional characterization of inhibitory and excitatory synaptic dysfunction in the *Ank3* W1989R mouse model may inform the future development of novel therapeutics for the treatment of BD and other neurological diseases involving altered excitatory/inhibitory balance.

ANK3 variants have been associated with schizophrenia [51], autism [52], epilepsy [40], and intellectual disability in addition to BD [53]. Variants in *ANK3* may contribute to these neurological diseases by affecting ankyrin-G expression levels, disrupting protein folding, impacting specific splice variants, or preventing ankyrin-G from interacting with critical-binding partners, as observed for GABARAP in the *Ank3* W1989R mouse model. Thus, it remains important to understand how disease-associated variants in *ANK3* affect ankyrin-G function and contribute to disease pathology. Although *ANK3* W1989R is a rare variant, the data reported in this work may have broader impacts on BD patients carrying other variants that reduce ankyrin-G expression. Several independent GWAS studies revealed *ANK3* BD-associated SNPs near the 5′ non-coding region, which could potentially lead to altered expression levels of different isoforms of ankyrin-G [36, 54–56]. Moreover, studies using postmortem brains from BD patients found reduced *ANK3* mRNA expression [57, 58]. Alternatively, a recent study also identified a SNP (rs41283526) in *ANK3* with a strong protective effect against BD [59]. Consistent with the *ANK3* W1989R variant, BD-associated rare variants have been detected within alternatively spliced exons of ankyrin-G [60]. One potential explanation to describe the genetic etiology of BD is that rare variants in *ANK3* have a high penetrance due to dysfunction of the gene or encoded splice variant. Alternatively, multiple common variants with low penetrance may lead to BD due to the polygenic nature of disease inheritance. In support of this hypothesis, rare variants in several genes involved in GABAergic and glutamatergic neurotransmission, as well as voltage-gated calcium channels contribute to increased risk of BD, as they may result in similar endophenotypes as individuals with *ANK3* mutations [61]. Ultimately, it will be important to continue to evaluate how patient-specific rare variants affect the expression and function of the different splice variants of ankyrin-G to provide insight on additional pathways that may contribute to BD and other neurological diseases.

Materials and methods

Constructs, protein expression, and purification

The coding sequence of the GABARAP (UniProt: Q9DCD6) construct was PCR amplified from a mouse brain cDNA library. The coding sequence of ankyrin-G construct was PCR amplified from the full-length rat 270 kDa ankyrin-G (UniProt: O70511) template. All point mutations were generated using the Quikchange II XL site-directed mutagenesis kit and confirmed by DNA sequencing. All of the constructs used for protein expression were cloned into a home-modified pET32a vector. Recombinant proteins were expressed in BL21 (DE3) *E. coli* cells with induction of 0.25 mM IPTG at 16 °C. The N-terminal Trx-His_6-tagged proteins were purified using Ni^{2+}-NTA agarose affinity columns followed by size-exclusion chromatography (Superdex 200 column from GE Healthcare) in the final buffer containing 50 mM Tris–HCl, 1 mM DTT, and 1 mM EDTA, pH 7.8 with 100 mM NaCl. The Trx-His_6 tag was removed by incubation with HRV 3C protease and separated by size-exclusion columns or reverse usage of Ni^{2+}-NTA columns when needed.

Crystallography

Crystallization of the ankyrin-G/GABARAP complex was performed using the sitting drop vapor diffusion method at 16 °C. Crystals of ankyrin-G/GABARAP were grown in solution containing 2.0 M ammonium citrate tribasic and 0.1 M Bis–Tris propane buffer (pH 7.0). Crystals were soaked in crystallization solution with higher salt concentration (3 M ammonium citrate) for dehydration and cryoprotection. All datasets were collected at the Shanghai Synchrotron Radiation Facility BL17U1 or BL19U1 beamline at 100 K. Data were processed and scaled using HKL2000 or HKL3000. Structure was solved by molecular replacement using PHASER with apo form structure of GABARAP (PDB: 1KJT) as the searching model. The ankyrin-G peptide was manually built according to the $F_o - F_c$ difference maps in COOT. Further manual model adjustment and refinement were completed iteratively using COOT and PHENIX. The final model was validated by MolProbity and statistics are summarized in Table 1. All structure figures were prepared by PyMOL (http://www.pymol.org).

Isothermal titration calorimetry (ITC) assay

ITC measurements were carried out on a VP-ITC Microcal calorimeter at 25 °C with the titration buffer containing 50 mM Tris–HCl, pH 7.8, 100 mM NaCl, 1 mM DTT, and 1 mM EDTA. For a typical experiment, each titration point was performed by injecting a 10 μL aliquot of protein sample (200 μM) into the cell containing another reactant (20 μM) at a time interval of 120 s to ensure that the titration peaks returned to the baseline. Twenty-seven aliquots were titrated in each individual experiment. The titration data were analyzed using the program Origin 7.0 and fitted by the one-site binding model.

Generation of *Ank3* W1989R mouse model

A knock-in mouse was generated by inserting the tryptophan to arginine mutation corresponding to human W1989R within the neuronal-specific giant exon of the mouse *Ank3* gene, which corresponds to exon 37 of human *ANK3*, ENST00000280772. The exon 37 plasmid contained the W1989R mutation and a neomycin resistance cassette. The neomycin resistance cassette was flanked by LoxP sites containing flippase recognition target (FRT) sites. The linearized construct was introduced into 129S6/SvEvTac-derived TL1 embryonic stem (ES) cells by electroporation. ES cells selected for the W1989R mutation using neomycin were injected into C57BL/6NHsd blastocysts. High percentage chimeric animals were obtained and bred to C57BL/6NHsd mice to produce heterozygous animals. The neo cassette was excised by crossing with the W1989R *Ank3* mouse containing a floxed neo cassette with a Sox2-Cre mouse [B6.Cg-Tg(Sox-cre)1Amc/J, stock number 008454; The Jackson Laboratory]. Mutant mice were backcrossed for at least six generations to C57BL6/J mice from the Jackson Laboratory and were compared to C57BL/6J mice as WT controls. Males and females were used for all experiments, and the order of mice used for experiments was randomized. Biological replicate number was based on previously published effects of ankyrin-G loss-of-function. All mouse production was provided by the Duke Cancer Institute Transgenic Mouse Facility. All experiments were performed in accordance with the guidelines for animal care of the Institutional Animal Care and Use Committee (IACUC) and University Laboratory Animal Management (ULAM) at the University of Michigan.

Immunocytochemistry of brain sections

For immunohistochemistry, P30–35 mice were administered a ketamine/xylazine mixture (80 mg/kg body weight ketamine and 10 mg/kg xylazine) via intraperitoneal injection. The mice were sacrificed by cardiac perfusion of PBS followed by 4% paraformaldehyde and the brain was immediately removed and fixed overnight in 4% paraformaldehyde. The next day, the brains were processed using a standard single-day paraffin preparation protocol (PBS wash followed by dehydrations through 70%, 95%, and 100% ethanol with final incubations in xylene and hot paraffin under vacuum) using a Leica ASP 300 paraffin tissue processor. Paraffin sections were cut 7 µm thick using a Leica RM2155 microtome and placed on glass slides. Sections were deparaffinized and rehydrated using a standard protocol of washes: 3 × 4-min xylene washes, 2 × 2-min 100% ethanol washes, and 1 × 2-min 95%, 80%, and 70% ethanol washes followed by at least 5 min in ddH_2O. Antigen retrieval was then conducted by microwaving the deparaffinized brain sections for 20 min in 10 µM sodium citrate. Sections were cooled, washed for 15 min in ddH_2O, rinsed in PBS for 5 min, and blocked using blocking buffer (5% BSA, 0.2% Tween 20 in PBS) for 1 h at room temperature. Slides were incubated overnight at 4 °C with primary antibodies diluted in blocking buffer. On the following day, slides were washed three times for 15 min with PBS containing 0.2% Tween 20, incubated with secondary antibodies diluted in blocking buffer for 1 h at room temperature, washed three times for 15 min, and mounted with Prolong Gold. AIS length was measured using maximum intensity projections of z-stacks. We only quantified AISs which were entirely contained within the bounds of the Z-stack. *N* refers to the number of mice used in the experiment, whereas *n* refers to the total number of AISs measured. To measure dendritic spine density in vivo, we used coronal brain slices (300–350 µm thick) and filled 1–2 CA1 hippocampal neurons/slice using whole-cell patch clamp with 2% biocytin in the internal solution. The brain slices were then incubated in 4% paraformaldehyde at 4 °C for 48 h, washed three times for 15 min with 0.1 M PBS at room, and blocked using 10% blocking serum (0.3% Triton X-100 and 10% of 5% BSA + 0.2% Tween in 0.1 M PBS) for 1 h at room temperature. The brain slices were then incubated in Streptavidin-594 nm (1:1000 dilution in blocking serum) overnight at 4 °C. The next day slices were washed three times for 15 min at room temperature, mounted on glass slides with Prolong Gold, and imaged on a Zeiss LSM 880 with a ×63 NA1.4 Oil/DIC Plan-Apochromat objective and 561 nm lasers. Images were pseudocolored white. Initial scoring or confirmation was done by investigators blinded to genotype.

Neuronal culture and transfection

Hippocampi were dissected from postnatal day 0 (P0) mice, treated with 0.25% trypsin and 100 µg/mL DNase in 2 mL HBSS with 10 mM HEPES, and then gently triturated through a glass pipette with a fire-polished tip. The dissociated neurons were then plated on poly-D-lysine and laminin-coated 35 mm MatTek dishes in 0.5 mL of Neurobasal-A medium containing 10% (vol/vol) FBS, B27 supplement, 2 mM glutamine, and penicillin/streptomycin. On the following day, 2.5 mL of fresh Neurobasal-A medium containing 1% FBS, B27, glutamine, and penicillin/streptomycin was added to the dish. AraC was added at 1:1000 to protect against glial and fibroblast overgrowth. Plates were returned to incubation at 37 °C until experimentation. To fill the cells with soluble GFP, the dissociated hippocampal cultures were transfected with eGFPN1 plasmid. Briefly, 1 µg eGFPN1 plasmid was added to 100 µL of Neurobasal-A and, in a second tube, 3 µL of Lipofectamine

2000 was added to 100 µL of Neurobasal-A. The two tubes were mixed and incubated for 15 min at room temperature. The neuronal growth media was then aspirated from the dishes and saved, the transfection was added dropwise to 14 DIV neurons, and the transfected cells were incubated at 37 °C for 1 h. The transfection mixture was aspirated and the original neuronal growth media was added. The cells were maintained in culture until 21 DIV and fixed for immunofluorescence as described below.

Immunofluorescence of cultured neurons

Dissociated hippocampal neurons were fixed for 15 min at room temperature with 4% paraformaldehyde, followed by methanol for 10 min at −20 °C, and blocked with blocking buffer (5% BSA, 0.2% Tween 20 in PBS). Primary antibodies were diluted in blocking buffer and incubated at 4 °C overnight. The following day, cells were washed three times for 15 min with PBS containing 0.2% Tween 20, incubated with secondary antibodies diluted in blocking buffer for 1 h at room temperature, washed three times for 15 min, and mounted with Prolong Gold.

Confocal microscopy

Samples were imaged on a Zeiss LSM 880 with a ×63 NA1.4 Oil/DIC Plan-Apochromat objective and excitation was accomplished using 405, 488, 561, and 633 nm lasers.

In vitro electrophysiology recordings and analysis

Brains were obtained from WT C57BL/6J or *Ank3* W1989R mutant mice between P25–48. The animals were decapitated under isoflurane and USP anesthesia, the brain was then quickly removed from the skull and placed in 4 °C slicing solution containing 62.5 mM NaCl, 2.5 mM KCl, 1.25 mM KH_2PO_4, 26 mM $NaHCO_3$, 5 mM $MgCl_2$, 0.5 mM $CaCl_2$, 20 mM glucose, and 100 mM sucrose (pH maintained at 7.4 by saturation with O_2/CO_2, 95/5%, respectively). Coronal brain slices (300–350 µm thick) containing layers II/III somatosensory cortex and hippocampus were cut with a microtome (VF-300, Compresstome). The slices were then transferred to a holding chamber and maintained at room temperature in artificial cerebrospinal fluid (ACSF) containing 125 mM NaCl, 2.5 mM KCl, 1.25 mM KH_2PO_4, 26 mM $NaHCO_3$, 1 mM $MgCl_2$, 2 mM $CaCl_2$, and 20 mM glucose, pH 7.4 (with 95%O_2 and 5%CO_2 bubbling through the solution) for at least 1 h prior to recording. After equilibration, individual slices were transferred to the recording chamber continuously perfused with ACSF (1–2 mL/min). Recording micropipettes were pulled from borosilicate glass capillaries (1.5 mm O.D. Harvard Apparatus) for a final resistance of 3–6 MΩ and filled with a solution containing 135 mM K-Gluconate, 4 mM NaCl, 0.4 mM GTP, 2 mM Mg-ATP,0.5 mM $CaCl_2$, 5 mM EGTA, and 10 mM HEPES. The signals were recorded with an Axoclamp 700B amplifier (Axon Instruments, Union City, CA), low-pass filtered at 10 kHz. Current clamp recordings were obtained from neurons in layers II/III of somatosensory cortex, CA1 hippocampus, the thalamus, and the cerebellum; the cells in these brain regions were identified using a Nikon Eclipse FN-1 microscope with a ×40 water-immersion objective and a DAGE-MTI IR-1000 video camera. Neurons were characterized using IR-DIC to evaluate their orientation, morphology, and spiking properties. Pyramidal neurons used for AP recordings exhibited prominent spike frequency patterns. We also recorded from fast-spiking, irregular spiking, and regular spiking non-pyramidal neurons as previously described [62]. Whole-cell patch-clamp recordings with a high cell resistance (>8 GΩ before break-in) were obtained for cells according to the availability. The neurons were characterized electrophysiologically by applying negative and positive current pulses of 20 pA and 1500 ms to calculate the maximum frequency and positive pulses of 50 ms to measure the features for the single AP. For sIPSC and mIPSC recordings in voltage-clamp configuration, the K-gluconate in the internal solution was replaced by CsCl and the recordings were acquired at 2 kHz fixing the voltage at −80 mV. The IPSCs were recorded in the presence of the N-methyl-D-aspartate receptor blockers and non-N-methyl-D-aspartate glutamate receptors, AP-5 (50 mM) and CNQX (10 µM). For measurement of mIPSCs, 1 µM TTX was added to the superfusion to block synaptic responses dependent on the AP. Access resistance was monitored throughout the experiment and experiments were canceled if changes > 20% occurred. The mEPSCs were measured in the presence of bicuculline (10 µM) and TTX (1 µM) while holding the resting membrane potential at −70 mV using K-gluconate internal solution. The peak events were searched automatically using Minianalysis (Synaptosoft Inc.) and visually monitored to exclude erroneous noise. Both the frequency and amplitude of the events and their distribution were analyzed. Mean values were compared using the Student's *t*-test. All data are presented as mean ± SEM.

In vitro kainate-induced oscillations

WT C57BL/6J or *Ank3* W1989R mice between P25–40 were anesthetized with isoflurane. Mice were perfused intracardially with ice cold (4 °C) modified N-methy-D-glucamine (NMDG) HEPES ACSF consisting of: 93 mM NMDG 2.5 mM KCl, 0.5 mM $CaCl_2$, 10 mM $MgCl_2$, 1.2 smM NaH_2PO_4, 20 mM HEPES, 25 mM dextrose, 5 mM ascorbic acid, 2 mM thiourea, and 3 mM Na-pyruvate. pH was maintained at 7.4 by saturation with O_2/CO_2 (95/5%,

respectively). Horizontal hippocampal sections (300 µm thick) were prepared with a Leica VT1200 vibratome. Sections were bi-laterally hemisected and transferred to a holding chamber maintained at 33 °C for 10–12 min, and then transferred to a holding chamber with aCSF consisting of: 126 mM NaCl, 3 mM KCl, 2 mM $CaCl_2$, 1 mM $MgCl_2$, 1.25 mM NaH_2PO_4, 25 mM $NaHCO_3$, and 10 mM dextrose. pH was maintained at 7.4 by saturating aCSF with 95%O_2/5% CO_2 at 33 °C for 35 min. Sections were then transferred to room temperature for 15 min and were mounted on perforated multi-electrode array (pMEAs) (Multichannel Systems, Reutlingen, Germany). Sections were secured to the surface of the pMEA surface by using a peristaltic perfusion system (PPS2, Multichannel Systems, Reutlingen, Germany) to create a slight vacuum through the perforations. The secured sections remained submerged in aCSF (29−31 °C, 95% O_2/5CO_2%) and were superfused at a rate of 5–7 mL/min. Local field potentials were recorded at 20 kHz. Baseline recordings were obtained for 1 h. Chemically induced oscillations were evoked by bath application of 400 nM kainic acid (KA) for 1 h. LFP data were imported into MATALAB, downsampled to 10 kHz and low-pass filtered at 400 Hz for analysis. Fast Fourier transformation (FFT) of LFP data was done in 1 s bins to calculate the power of oscillations. Sonograms are plotted as the average power in a 2 min window and the last 2 min of each bath condition were used for further analysis. Change in oscillatory power was defined as $(Power_{KA} - Power_{aCSF})/Power_{aCSF}$. Peak frequency and the area under the curve for gamma band (30–60 Hz) were calculated using custom written MATLAB scripts.

Western blot

Homogenization buffer consisting of 8 M urea, 5% SDS, and 5 mM N-ethylmaleimide was heated to 65 °C. Whole brains were dissected from P30–35 mice and immediately frozen in liquid nitrogen. Frozen brains were then ground into a powder using a mortar and pestle. The powder was scraped into a 1.5 mL microcentrifuge tube and hand-dounced in 10 volumes/weight of 65 °C homogenization buffer (i.e. 1.5 mL for 150 mg powder). The homogenate was incubated at 65 °C for 20 min and then mixed 1:1 with 5× PAGE buffer (5% (wt/vol) SDS, 25% (wt/vol) sucrose, 50 mM Tris, pH 8, 5 mM EDTA, bromophenol blue). The lysates were stored at −80 °C until use. The samples (10 µL volume) were separated on a 3.5–17% gradient gel in 1× Tris buffer, pH 7.4 (40 mM Tris, 20 mM NaOAc, and 2 mM NaEDTA) with 0.2% SDS. Transfer to nitrocellulose was performed overnight at 300 mA at 4 °C in 0.5× Tris buffer with 0.01% SDS. Membranes were blocked with 5% Bovine Serum Albumin (BSA) in TBS and incubated overnight at 4 °C with primary antibodies (rabbit total ankyrin-G 1:5,000) diluted in blocking buffer. Membranes were washed 3× 15 min with TBS-T and incubated for 1 h with LiCor fluorescent secondaries (1:50,000) in blocking buffer. Membrane were then washed 3× 15 min in TBS-T, 1× 5 min TBS, and 1× 5 min in ddH_2O before being imaged on LiCor Odyssey Clx imager.

Antibodies and reagents

The following antibodies and dilutions were used: rabbit anti-βIV-spectrin (1:1000, lab-generated [16]), rabbit anti-total ankyrin-G (1:1000, lab-generated [63]), goat anti-total ankyrin-G (1:1000, lab-generated [16]), rabbit anti-KCNQ2N1 (1:500 [64]), rabbit anti-NaV (1:500, Sigma S6936), rabbit anti-neurofascin FNIII (1:500, lab generated [65]), mouse anti-NeuN (1:1000, Sigma MAB377), mouse anti-caspr (1:1000, Neuromab 75–001), guinea pig anti-vGAT (1:1000, Synaptic Systems 131004), mouse anti-$GABA_A$ receptor β2-3 (1:1000, Sigma, MAB341), mouse anti-parvalbumin (1:1000, Sigma P3088), and rabbit anti-calbindin (1:1000, Swant CB-38a). Antibodies against KCNQ2 were used to label heteromeric KCNQ2/3 channels at the AIS [64]. Fluorescently conjugated secondary antibodies Alexa Fluor 488, 568, or 647 (1:250, Life Technologies) and Alexa Fluor 594-Streptavidin (1:1000, Jackson ImmunoResearch 016-580-084). The following reagents were used: FBS, poly-D-lysine, laminin, paraformaldehyde, DNase, urea, and N-ethylmaleimide were from Sigma-Aldrich. B27 supplement, GlutaMAX, Penicillin–Streptomycin, Neurobasal-A, Hank's balanced salt solution, trypsin, hepes, lipofectamine 2000 and Prolong Gold Antifade Reagent were from Life Technologies. Bovine serum albumin was from Gemini Bioproducts. Tween 20 was from Calbiochem.

Image acquisition and statistical analysis

Multi-color imaging was performed as previously described using a Zeiss 880 confocal microscope [16]. All images were further processed in Adobe Photoshop CC 2018 software. Statistical analyses were performed using Microsoft Excel and GraphPad Prism 7. A confidence interval of 95% ($P < 0.05$) was required for values to be considered statistically significant. All *t* tests were two-tailed. All data are presented as mean ± SEM. Biological replicates (animals) indicated by capital N and individual measurements indicated by lowercase n.

Subjects, sequencing, and genotyping

All subjects were identified with IRB approval (University of Michigan IRBMed) through the Heinz C. Prechter

Bipolar Research Program at the University of Michigan. This program is the largest privately funded longitudinal study of BD, which monitors BD patients for 10 years and beyond following an initial evaluation, bi-monthly questionnaires, and neuropsychological testing by a clinical psychiatrist. The proband (II:1) was initially identified using whole genome and exome sequencing of blood samples from the Prechter Bipolar Genetics Repository at the University of Michigan. We confirmed the *ANK3* W1989R variant (rs372922084, c.5965T>C (p.Trp1989Arg) by extracting DNA from a fibroblast biopsy under IRB from the proband and performing a nested PCR initially using the primer pair 5′-GTAGCTGAAATGAAAGAGGACCT-3′ and 5′-TCTCAGAGGTGGAAGTCCTC-3′ then 5′-GATGATGAAGAACCTTTCAAAATTG-3′ and 5′-GAGGCATTTTGAGTTTGTGTTC-3′. Blood was then drawn from the mother (I:2) and father (I:1) under IRB. We extracted the DNA and performed a nested PCR using the same primers listed above. DNA from the sister (II:1) was provided from the University of Michigan Central Biorepository as part of the Heinz C. Prechter Bipolar Research Program. The 500 bp PCR fragments were purified following gel electrophoresis using a gel extraction kit and sent for sequencing at the University of Michigan DNA sequencing core. All subjects reported Caucasian ancestry. The clinical data is from a detailed clinical interview using an established instrument, the Diagnostic Interview for Genetics Studies (DIGS) [66]. The interview was conducted by a Ph.D. or M.D. level clinician and reviewed by two independent M.D./Ph.D. level faculty who had access to all available medical records, including those from treating physicians. Informed consent was obtained from all patients.

Data availability

Atomic coordinates and structure factors are available from the Protein Data Bank under accession code PDB A9X (AnkG/GABARAPL).

Acknowledgements We thank the Shanghai Radiation Facility BL19U1 and BL17U1 for X-ray beam time. Funding for this work was provided by the Michigan Predoctoral Training in Genetics (T32GM007544) (ADN), NIH Early Stage Training in the Neurosciences Training Grant (T32NS076401) (JCRD and JMH), Heinz C. Prechter Bipolar Research program and Richard Tam Foundation, University of Michigan Depression Center (PMJ), R37NS076752 (LLI), National Natural Science Foundation of China (NSFC 31670734) (CW), Research Grants Council of Hong Kong (16100517 and AoE-M09-12) (MZ), R01DA020140 (KSJ), and the Howard Hughes Medical Institute (VB). Finally, we thank Dr. Ed Cooper (Baylor College of Medicine) for providing the KCNQ2N1 antibody.

Author contributions ADN, RNFC, CW, MZ, KSJ, LLS, LLI, and PMJ designed research. PMJ, KKW, KC, and VB generated and initially characterized the *Ank3* W1989R mutant mice. ADN, RNCF, JCRD, JMH, YY, JL, KC, and CW performed experiments. ADN, RNCF, JCRD, CW, MZ, KSJ, and PMJ analyzed data. MMG provided human samples and clinical diagnosis. ADN and PMJ wrote the manuscript.

Compliance with ethical standards

Conflict of interest The authors declare that they have no conflict of interest.

References

1. Benes FM. Amygdalocortical circuitry in schizophrenia: from circuits to molecules. Neuropsychopharmacology. 2010;35:239–57.
2. Benes FM, Berretta S. GABAergic interneurons: implications for understanding schizophrenia and bipolar disorder. Neuropsychopharmacology. 2001;25:1–27.
3. Konradi C, Zimmerman EI, Yang CK, Lohmann KM, Gresch P, Pantazopoulos H, et al. Hippocampal interneurons in bipolar disorder. Arch Gen Psychiatry. 2011;68:340–50.
4. Lazarus MS, Krishnan K, Huang ZJ. GAD67 deficiency in parvalbumin interneurons produces deficits in inhibitory transmission and network disinhibition in mouse prefrontal cortex. Cereb Cortex. 2015;25:1290–6.
5. Ozerdema A, Guntekind B, Atagune MI, Basar E. Brain oscillations in bipolar disorder in search of new biomarkers. Suppl Clin Neurophysiol. 2013;62:207–21.
6. Schubert KO, Focking M, Cotter DR. Proteomic pathway analysis of the hippocampus in schizophrenia and bipolar affective disorder implicates 14-3-3 signaling, aryl hydrocarbon receptor signaling, and glucose metabolism: potential roles in GABAergic interneuron pathology. Schizophr Res. 2015;167:64–72.
7. Sohal VS. Insights into cortical oscillations arising from optogenetic studies. Biol Psychiatry. 2012;71:1039–45.
8. Torrey EF, Barci BM, Webster MJ, Bartko JJ, Meador-Woodruff JH, Knable MB. Neurochemical markers for schizophrenia, bipolar disorder, and major depression in postmortem brains. Biol Psychiatry. 2005;57:252–60.
9. Bennett V, Lorenzo DN. Spectrin- and ankyrin-based membrane domains and the evolution of vertebrates. Curr Top Membr. 2013;72:1–37.
10. Nelson AD, Jenkins PM. Axonal membranes and their domains: assembly and function of the axon initial segment and node of Ranvier. Front Cell Neurosci. 2017;11:136.
11. Kordeli E, Lambert S, Bennett V, Ankyrin G. A new ankyrin gene with neural-specific isoforms localized at the axonal initial segment and node of Ranvier. J Biol Chem. 1995;270:2352–9.
12. Nelson AD, Jenkins PM. Axonal membranes and their domains: assembly and function of the axon initial segment and node of Ranvier. Front Cell Neurosci. 2017;11:136.
13. Tseng WC, Jenkins PM, Tanaka M, Mooney R, Bennett V. Giant ankyrin-G stabilizes somatodendritic GABAergic synapses through opposing endocytosis of GABAA receptors. Proc Natl Acad Sci USA. 2015;112:1214–9.
14. Chen ZW, Olsen RW. GABAA receptor associated proteins: a key factor regulating GABAA receptor function. J Neurochem. 2007;100:279–94.
15. Alemu EA, Lamark T, Torgersen KM, Birgisdottir AB, Larsen KB, Jain A, et al. ATG8 family proteins act as scaffolds for assembly of the ULK complex: sequence requirements for LC3-interacting region (LIR) motifs. J Biol Chem. 2012;287:39275–90.
16. Jenkins PM, Kim N, Jones SL, Tseng WC, Svitkina TM, Yin HH, et al. Giant ankyrin-G: a critical innovation in vertebrate evolution

of fast and integrated neuronal signaling. Proc Natl Acad Sci USA. 2015;112:957–64.
17. Li J, Zhu R, Chen K, Zheng H, Zhao H, Yuan C, et al. Potent and specific Atg8-targeting autophagy inhibitory peptides from giant ankyrins. Nat Chem Biol. 2018;14:778–87.
18. Rogov VV, Stolz A, Ravichandran AC, Rios-Szwed DO, Suzuki H, Kniss A, et al. Structural and functional analysis of the GABARAP interaction motif (GIM). EMBO Rep. 2017;18:1382–96.
19. Jenkins PM, Vasavda C, Hostettler J, Davis JQ, Abdi K, Bennett V. E-cadherin polarity is determined by a multifunction motif mediating lateral membrane retention through ankyrin-G and apical-lateral transcytosis through clathrin. J Biol Chem. 2013;288:14018–31.
20. Rudy B, Fishell G, Lee S, Hjerling-Leffler J. Three groups of interneurons account for nearly 100% of neocortical GABAergic neurons. Dev Neurobiol. 2011;71:45–61.
21. Somogyi P, Katona L, Klausberger T, Lasztoczi B, Viney TJ. Temporal redistribution of inhibition over neuronal subcellular domains underlies state-dependent rhythmic change of excitability in the hippocampus. Philos Trans R Soc Lond B Biol Sci. 2014;369:20120518.
22. Sohal VS, Zhang F, Yizhar O, Deisseroth K. Parvalbumin neurons and gamma rhythms enhance cortical circuit performance. Nature. 2009;459:698–702.
23. Tamas G, Buhl EH, Lorincz A, Somogyi P. Proximally targeted GABAergic synapses and gap junctions synchronize cortical interneurons. Nat Neurosci. 2000;3:366–71.
24. Fogarty M, Grist M, Gelman D, Marin O, Pachnis V, Kessaris N. Spatial genetic patterning of the embryonic neuroepithelium generates GABAergic interneuron diversity in the adult cortex. J Neurosci. 2007;27:10935–46.
25. Buzsaki G, Wang XJ. Mechanisms of gamma oscillations. Annu Rev Neurosci. 2012;35:203–25.
26. Cardin JA, Carlen M, Meletis K, Knoblich U, Zhang F, Deisseroth K, et al. Driving fast-spiking cells induces gamma rhythm and controls sensory responses. Nature. 2009;459:663–7.
27. Fisahn A, Contractor A, Traub RD, Buhl EH, Heinemann SF, McBain CJ. Distinct roles for the kainate receptor subunits GluR5 and GluR6 in kainate-induced hippocampal gamma oscillations. J Neurosci. 2004;24:9658–68.
28. Marin O. Interneuron dysfunction in psychiatric disorders. Nat Rev Neurosci. 2012;13:107–20.
29. Lin YC, Koleske AJ. Mechanisms of synapse and dendrite maintenance and their disruption in psychiatric and neurodegenerative disorders. Annu Rev Neurosci. 2010;33:349–78.
30. Smith KR, Kopeikina KJ, Fawcett-Patel JM, Leaderbrand K, Gao R, Schurmann B, et al. Psychiatric risk factor ANK3/ankyrin-G nanodomains regulate the structure and function of glutamatergic synapses. Neuron. 2014;84:399–415.
31. Lek M, Karczewski KJ, Minikel EV, Samocha KE, Banks E, Fennell T, et al. Analysis of protein-coding genetic variation in 60,706 humans. Nature. 2016;536:285–91.
32. Goes FS, Pirooznia M, Parla JS, Kramer M, Ghiban E, Mavruk S, et al. Exome Sequencing of Familial Bipolar Disorder. JAMA Psychiatry. 2016;73:590–7.
33. Harrison PJ, Geddes JR, Tunbridge EM. The emerging neurobiology of bipolar disorder. Trends Neurosci. 2017;41:18–30.
34. Hatzimanolis A, Smyrnis N, Avramopoulos D, Stefanis CN, Evdokimidis I, Stefanis NC. Bipolar disorder ANK3 risk variant effect on sustained attention is replicated in a large healthy population. Psychiatr Genet. 2012;22:210–3.
35. Leussis MP, Madison JM, Petryshen TL. Ankyrin 3: genetic association with bipolar disorder and relevance to disease pathophysiology. Biol Mood Anxiety Disord. 2012;2:18.
36. Schulze TG, Detera-Wadleigh SD, Akula N, Gupta A, Kassem L, Steele J, et al. Two variants in Ankyrin 3 (ANK3) are independent genetic risk factors for bipolar disorder. Mol Psychiatry. 2009;14:487–91.
37. Yamada R, Kuba H. Structural and functional plasticity at the axon initial segment. Front Cell Neurosci. 2016;10:250.
38. Ango F, di Cristo G, Higashiyama H, Bennett V, Wu P, Huang ZJ. Ankyrin-based subcellular gradient of neurofascin, an immunoglobulin family protein, directs GABAergic innervation at purkinje axon initial segment. Cell. 2004;119:257–72.
39. Zhu S, Cordner ZA, Xiong J, Chiu CT, Artola A, Zuo Y, et al. Genetic disruption of ankyrin-G in adult mouse forebrain causes cortical synapse alteration and behavior reminiscent of bipolar disorder. Proc Natl Acad Sci USA. 2017;114:10479–84.
40. Lopez AY, Wang X, Xu M, Maheshwari A, Curry D, Lam S, et al. Ankyrin-G isoform imbalance and interneuronopathy link epilepsy and bipolar disorder. Mol Psychiatry. 2017;22:1464–72.
41. Leussis MP, Berry-Scott EM, Saito M, Jhuang H, de Haan G, Alkan O, et al. The ANK3 bipolar disorder gene regulates psychiatric-related behaviors that are modulated by lithium and stress. Biol Psychiatry. 2013;73:683–90.
42. Benes FM, Lim B, Matzilevich D, Walsh JP, Subburaju S, Minns M. Regulation of the GABA cell phenotype in hippocampus of schizophrenics and bipolars. Proc Natl Acad Sci USA. 2007;104:10164–9.
43. Glantz LA, Lewis DA. Decreased dendritic spine density on prefrontal cortical pyramidal neurons in schizophrenia. Arch Gen Psychiatry. 2000;57:65–73.
44. Konopaske GT, Lange N, Coyle JT, Benes FM. Prefrontal cortical dendritic spine pathology in schizophrenia and bipolar disorder. JAMA Psychiatry. 2014;71:1323–31.
45. Lee Y, Zhang Y, Kim S, Han K. Excitatory and inhibitory synaptic dysfunction in mania: an emerging hypothesis from animal model studies. Exp Mol Med. 2018;50:12.
46. Ohgi Y, Futamura T, Hashimoto K. Glutamate signaling in synaptogenesis and NMDA receptors as potential therapeutic targets for psychiatric disorders. Curr Mol Med. 2015;15:206–21.
47. Penzes P, Buonanno A, Passafaro M, Sala C, Sweet RA. Developmental vulnerability of synapses and circuits associated with neuropsychiatric disorders. J Neurochem. 2013;126:165–82.
48. Penzes P, Cahill ME, Jones KA, VanLeeuwen JE, Woolfrey KM. Dendritic spine pathology in neuropsychiatric disorders. Nat Neurosci. 2011;14:285–93.
49. Chattopadhyaya B, Cristo GD. GABAergic circuit dysfunctions in neurodevelopmental disorders. Front Psychiatry. 2012;3:51.
50. Ozerdem A, Guntekin B, Saatci E, Tunca Z, Basar E. Disturbance in long distance gamma coherence in bipolar disorder. Prog Neuropsychopharmacol Biol Psychiatry. 2010;34:861–5.
51. Wirgenes KV, Tesli M, Inderhaug E, Athanasiu L, Agartz I, Melle I, et al. ANK3 gene expression in bipolar disorder and schizophrenia. Br J Psychiatry. 2014;205:244–5.
52. Kloth K, Denecke J, Hempel M, Johannsen J, Strom TM, Kubisch C, et al. First de novo ANK3 nonsense mutation in a boy with intellectual disability, speech impairment and autistic features. Eur J Med Genet. 2017;60:494–8.
53. Iqbal Z, Vandeweyer G, van der Voet M, Waryah AM, Zahoor MY, Besseling JA, et al. Homozygous and heterozygous disruptions of ANK3: at the crossroads of neurodevelopmental and psychiatric disorders. Hum Mol Genet. 2013;22:1960–70.
54. Craddock N, Sklar P. Genetics of bipolar disorder. Lancet. 2013;381:1654–62.
55. Ferreira MA, O'Donovan MC, Meng YA, Jones IR, Ruderfer DM, Jones L, et al. Collaborative genome-wide association analysis supports a role for ANK3 and CACNA1C in bipolar disorder. Nat Genet. 2008;40:1056–8.

56. Muhleisen TW, Leber M, Schulze TG, Strohmaier J, Degenhardt F, Treutlein J, et al. Genome-wide association study reveals two new risk loci for bipolar disorder. Nat Commun. 2014;5:3339.
57. Roussos P, Katsel P, Davis KL, Bitsios P, Giakoumaki SG, Jogia J, et al. Molecular and genetic evidence for abnormalities in the nodes of Ranvier in schizophrenia. Arch Gen Psychiatry. 2012;69:7–15.
58. Rueckert EH, Barker D, Ruderfer D, Bergen SE, O'Dushlaine C, Luce CJ, et al. Cis-acting regulation of brain-specific ANK3 gene expression by a genetic variant associated with bipolar disorder. Mol Psychiatry. 2013;18:922–9.
59. Hughes T, Hansson L, Sonderby IE, Athanasiu L, Zuber V, Tesli M, et al. A loss-of-function variant in a minor isoform of ANK3 protects against bipolar disorder and schizophrenia. Biol Psychiatry. 2016;80:323–30.
60. Doyle GA, Lai AT, Chou AD, Wang MJ, Gai X, Rappaport EF, et al. Re-sequencing of ankyrin 3 exon 48 and case-control association analysis of rare variants in bipolar disorder type I. Bipolar Disord. 2012;14:809–21.
61. Ament SA, Szelinger S, Glusman G, Ashworth J, Hou L, Akula N, et al. Rare variants in neuronal excitability genes influence risk for bipolar disorder. Proc Natl Acad Sci USA. 2015;112:3576–81.
62. Cauli B, Porter JT, Tsuzuki K, Lambolez B, Rossier J, Quenet B, et al. Classification of fusiform neocortical interneurons based on unsupervised clustering. Proc Natl Acad Sci USA. 2000;97:6144–9.
63. Kizhatil K, Yoon W, Mohler PJ, Davis LH, Hoffman JA, Bennett V. Ankyrin-G and beta2-spectrin collaborate in biogenesis of lateral membrane of human bronchial epithelial cells. J Biol Chem. 2007;282:2029–37.
64. Cooper EC, Harrington E, Jan YN, Jan LY. M channel KCNQ2 subunits are localized to key sites for control of neuronal network oscillations and synchronization in mouse brain. J Neurosci. 2001;21:9529–40.
65. Davis JQ, Lambert S, Bennett V. Molecular composition of the node of Ranvier: identification of ankyrin-binding cell adhesion molecules neurofascin (mucin+/third FNIII domain-) and NrCAM at nodal axon segments. J Cell Biol. 1996;135:1355–67.
66. Nurnberger JI Jr., Blehar MC, Kaufmann CA, York-Cooler C, Simpson SG, Harkavy-Friedman J, et al. Diagnostic interview for genetic studies. Rationale, unique features, and training. NIMH Genetics Initiative. Arch Gen Psychiatry. 1994;51:849–59. discussion 863-844

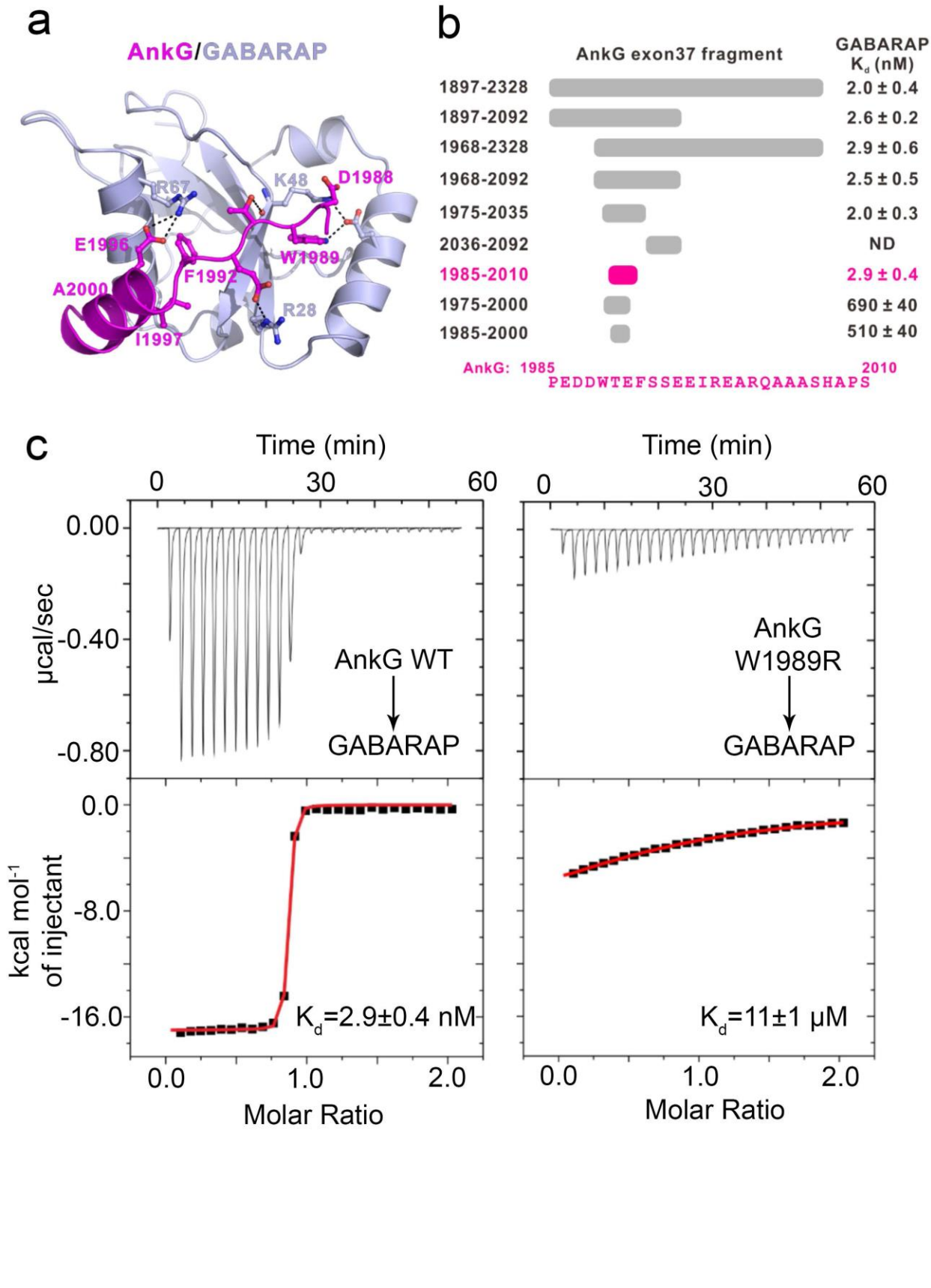
a
AnkG/GABARAP
R67
K48
D1988
E1996
W1989
F1992
A2000
R28
I1997
b
AnkG exon37 fragment
GABARAP
K$_d$ (nM)
1897-2328
2.0 ± 0.4
1897-2092
2.6 ± 0.2
1968-2328
2.9 ± 0.6
1968-2092
2.5 ± 0.5
1975-2035
2.0 ± 0.3
2036-2092
ND
1985-2010
2.9 ± 0.4
1975-2000
690 ± 40
1985-2000
510 ± 40
AnkG: 1985
2010
PEDDWTEFSSEEIREARQAAASHAPS
c
Time (min)
0
30
60
0.00
-0.40
-0.80
µcal/sec
AnkG WT
GABARAP
AnkG
W1989R
GABARAP
0.0
-8.0
-16.0
kcal mol^{-1}
of injectant
K$_d$=2.9±0.4 nM
K$_d$=11±1 µM
0.0
1.0
2.0
Molar Ratio

Supplementary Fig. 1: W1989 reside in ankyrin-G is necessary for high affinity binding to GABARAP.

(a) Ribbon representation of the ankyrin-G/GABARAP complex structure. Key residues critical for the binding are shown in the stick model. Salt bridges and hydrogen bonds are indicated with dashed lines. **(b)** Biochemical analysis of the complex formation between ankyrin-G and GABARAP. Isothermal Titration Calorimetry (ITC)-based mapping of the minimal region of the giant exon of ankyrin-G capable of binding to GABARAP. The minimal and complete fragment identified is highlighted in magenta, and the amino acid sequence of ankyrin-G 1985-2010 is listed at the bottom. “ND” denotes that the construct had no detectable binding to GABARAP. **(c)** ITC-derived binding curves of WT ankyrin-G and W1989R ankyrin-G to GABARAP.

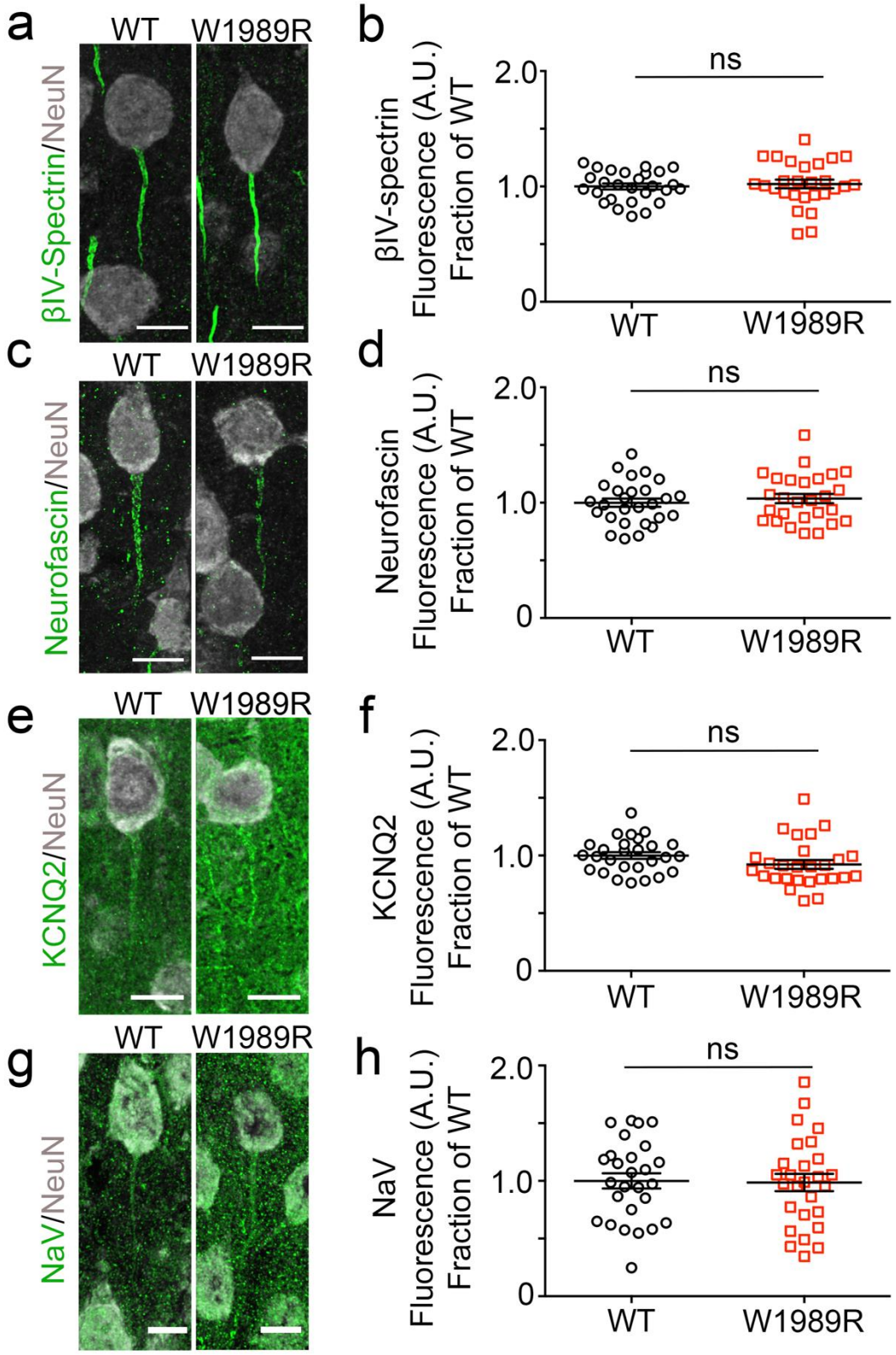
a
WT
W1989R
βIV-Spectrin/NeuN
b
βIV-spectrin
Fluorescence (A.U.)
Fraction of WT
ns
2.0
1.0
0
WT
W1989R
c
WT
W1989R
Neurofascin/NeuN
d
Neurofascin
Fluorescence (A.U.)
Fraction of WT
ns
2.0
1.0
0
WT
W1989R
e
WT
W1989R
KCNQ2/NeuN
f
KCNQ2
Fluorescence (A.U.)
Fraction of WT
ns
2.0
1.0
0
WT
W1989R
g
WT
W1989R
NaV/NeuN
h
NaV
Fluorescence (A.U.)
Fraction of WT
ns
2.0
1.0
0
WT
W1989R

Supplementary Fig. 2: W1989R 480 kDa ankyrin-G is capable of clustering all known ankyrin-G binding partners to the AIS.

(a) Representative images of the AIS of pyramidal neurons in layer II/III of the somatosensory cortex of P30 WT (left) and *Ank3* W1989R homozygous (right) mice. Coronal brain sections immunostained with βIV-spectrin (green) and NeuN (white). Scale bar: 10 µm. **(b)** Quantification of βIV-spectrin fluorescence intensity (a.u.) as fraction of WT between WT (black circles) and *Ank3* W1989R homozygous (red squares) mice. *t-test* P = 0.6375 (WT: 1 ± 0.03, N=3, n=27; W1989R: 1.02 ± 0.04, N=3, n=27). **(c)** Representative images of cortical pyramidal neuron AISs of P30 WT (left) and *Ank3* W1989R homozygous (right) mice immunostained with pan-neurofascin (green) and NeuN (white). Scale bar: 10 µm. **(d)** Quantification of neurofascin fluorescence intensity (a.u.) as fraction of WT between WT (black circles) and *Ank3* W1989R homozygous (red squares) mice. *t-test* P = 0.517 (WT: 1 ± 0.04, N=3, n=27; W1989R: 1.04 ± 0.04, N=3, n=27). **(e)** Representative images of cortical pyramidal neuron AISs of P30 WT (left) and *Ank3* W1989R homozygous (right) mice immunostained with KCNQ2 (green) and NeuN (white). Scale bar: 10 µm. **(f)** Quantification of KCNQ2 fluorescence intensity (a.u.) as fraction of WT between WT (black circles) and *Ank3* W1989R homozygous (red squares) mice. *t-test* P = 0.116 (WT: 1 ± 0.03, N=3, n=27; W1989R: 0.92 ± 0.03, N=3, n=27). **(g)** Representative images of cortical pyramidal neuron AISs of P30 WT (left) and *Ank3* W1989R homozygous (right) mice immunostained with pan-NaV (green) and NeuN (white). Scale bar: 10 µm. **(h)** Quantification of Nav fluorescence intensity (a.u.) as fraction of WT

between WT (black circles) and *Ank3* W1989R homozygous (red squares) mice. *t-test* P = 0.89 (WT: 1 ± 0.07, N=3, n=27; W1989R: 0.99 ± 0.07, N=3, n=27).

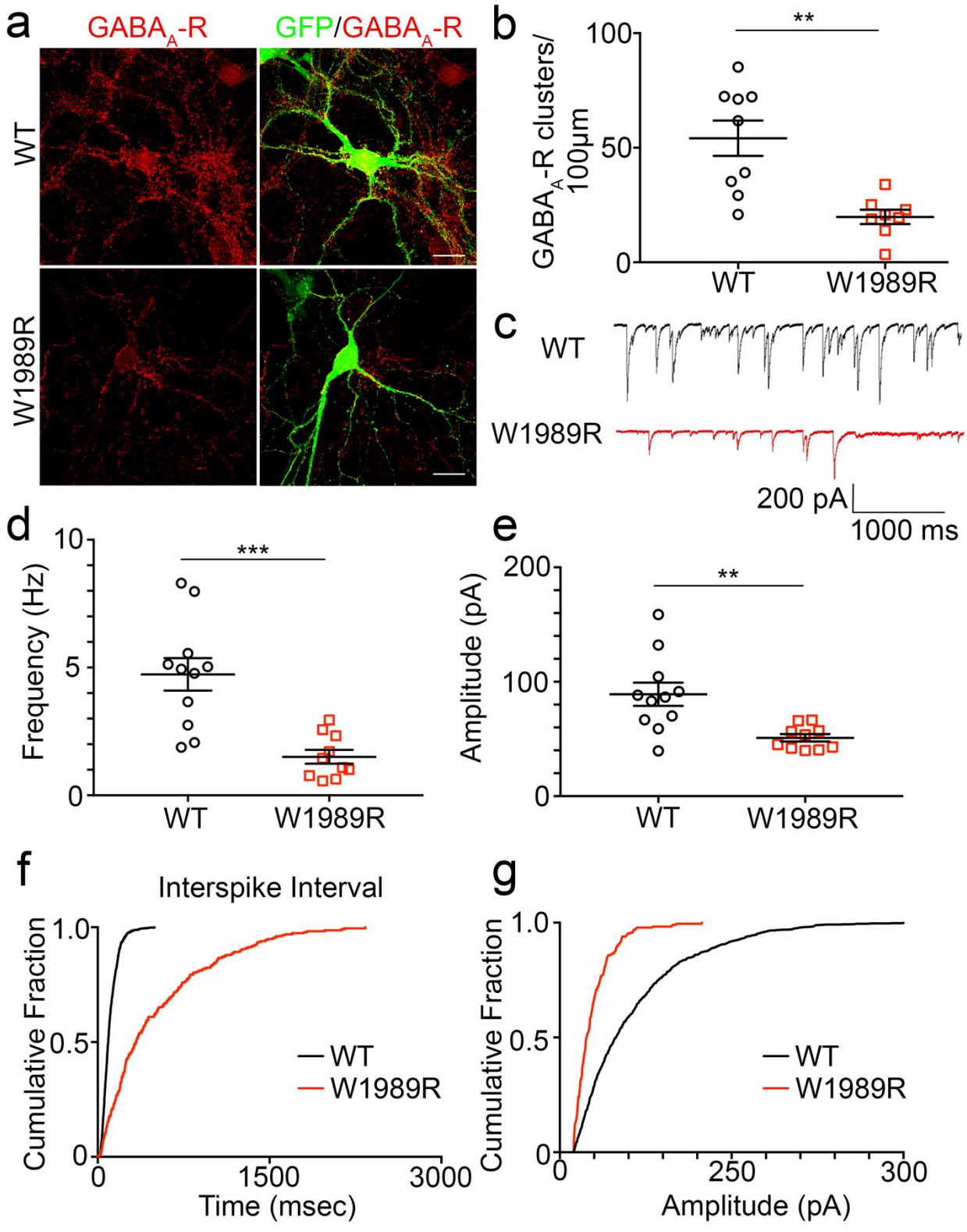
a
GABA$_A$-R
GFP/GABA$_A$-R
WT
W1989R
b
GABA$_A$-R clusters/ 100μm
100
50
0
**
WT
W1989R
c
WT
W1989R
200 pA
1000 ms
d
Frequency (Hz)
10
5
0
***
WT
W1989R
e
Amplitude (pA)
200
100
0
**
WT
W1989R
f
Interspike Interval
Cumulative Fraction
1.0
0.5
0
WT
W1989R
0
1500
3000
Time (msec)
g
Cumulative Fraction
1.0
0.5
0
WT
W1989R
0
250
300
Amplitude (pA)

Supplementary Fig. 3: Loss of pre- and post-synaptic GABAergic synapses in *Ank3* W1989R CA1 hippocampal neurons.

(a) Representative images of dissociated hippocampal cultured neurons at 21 DIV from WT (top) and *Ank3* W1989R homozygous (bottom) mice. Soluble GFP shown in green and immunostaining for $GABA_A$ receptor β2-3 subunit shown in red. Scale bar: 20 µm. **(b)** Quantification of the total number of $GABA_A$ receptor clusters per 100 µm per neuron. *t-test* **P = 0.0013 (WT: 54.1 ± 7.7, N=3, n=9; W1989R: 19.8 ± 3.1, N=3, n=8). **(c)** Spontaneous inhibitory post-synaptic current (sIPSC) representative traces from CA1 hippocampal neurons in WT (black) and *Ank3* W1989R (red) slices. Scale bars: 200 pA, 1000 ms. **(d)** Quantification of spontaneous inhibitory post-synaptic current (sIPSC) frequency in CA1 hippocampal neurons WT (black circles) and *Ank3* W1989R (red squares) brain slices. *t-test* ***P = 0.0002 (WT: 4.7 ± 0.6 Hz, n=11; W1989R: 1.5 ± 0.3 Hz, n=10). **(e)** Quantification of sIPSC amplitude in WT (black circles) and *Ank3* W1989R (red squares) CA1 hippocampal neurons in brain slices. *t-test* ***P = 0.0027 (WT: 89.1 ± 10.1 pA, n=11; W1989R: 51.0 ± 3.3 pA, n=10). **(f)** Cumulative histogram of interspike interval frequency (black line) and *Ank3* W1989R (red line) CA1 hippocampal neurons using whole cell voltage-clamp recording. *t-test* ****P < 0.0001.

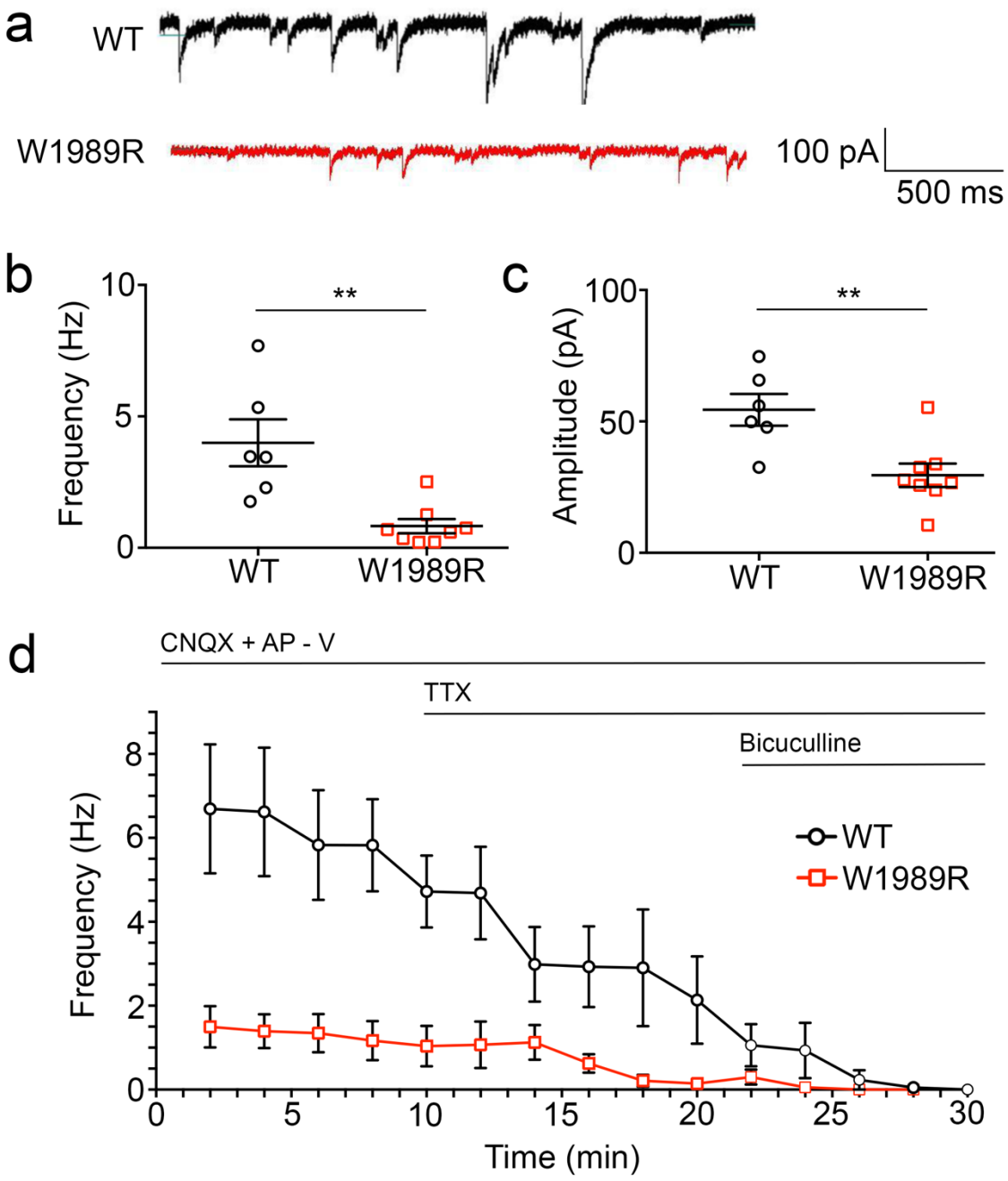
a
WT
W1989R
100 pA
500 ms
b
Frequency (Hz)
10
5
0
**
WT
W1989R
c
Amplitude (pA)
100
50
0
**
WT
W1989R
d
CNQX + AP - V
TTX
Bicuculline
WT
W1989R
Frequency (Hz)
8
6
4
2
0
0
5
10
15
20
25
30
Time (min)

Supplementary Fig. 4: Miniature inhibitory post-synaptic currents (mIPSCs) are decreased in *Ank3* W1989R cortical pyramidal neurons.

(a) Representative traces of miniature inhibitory post-synaptic currents (mIPSCs) of whole cell voltage-clamp recordings from layer II/III somatosensory cortical neurons in WT (black) and *Ank3* W1989R (red) homozygous brain slices. Scale bar: 100 pA, 500 ms. **(b)** Quantification of mIPSC frequency in WT (black circles) and *Ank3* W1989R homozygous (red squares) brain slices. *t-test* **P = 0.0023 (WT: 4.0 ± 0.9 Hz, n=6; W1989R: 0.83 ± 0.27 Hz, n=8). **(c)** Quantification of mIPSC amplitude in WT (black circles) and W1989R (red squares) brain slices. *t-test* **P = 0.0052 (WT: 54.4 ± 6.0 pA, n=6; W1989R: 29.5 ± 4.5 pA, n=8). **(d)** Quantification of IPSC frequency in response to tetrodotoxin (TTX) and bicuculline between WT (black circles) and *Ank3* W1989R homozygous (red squares).

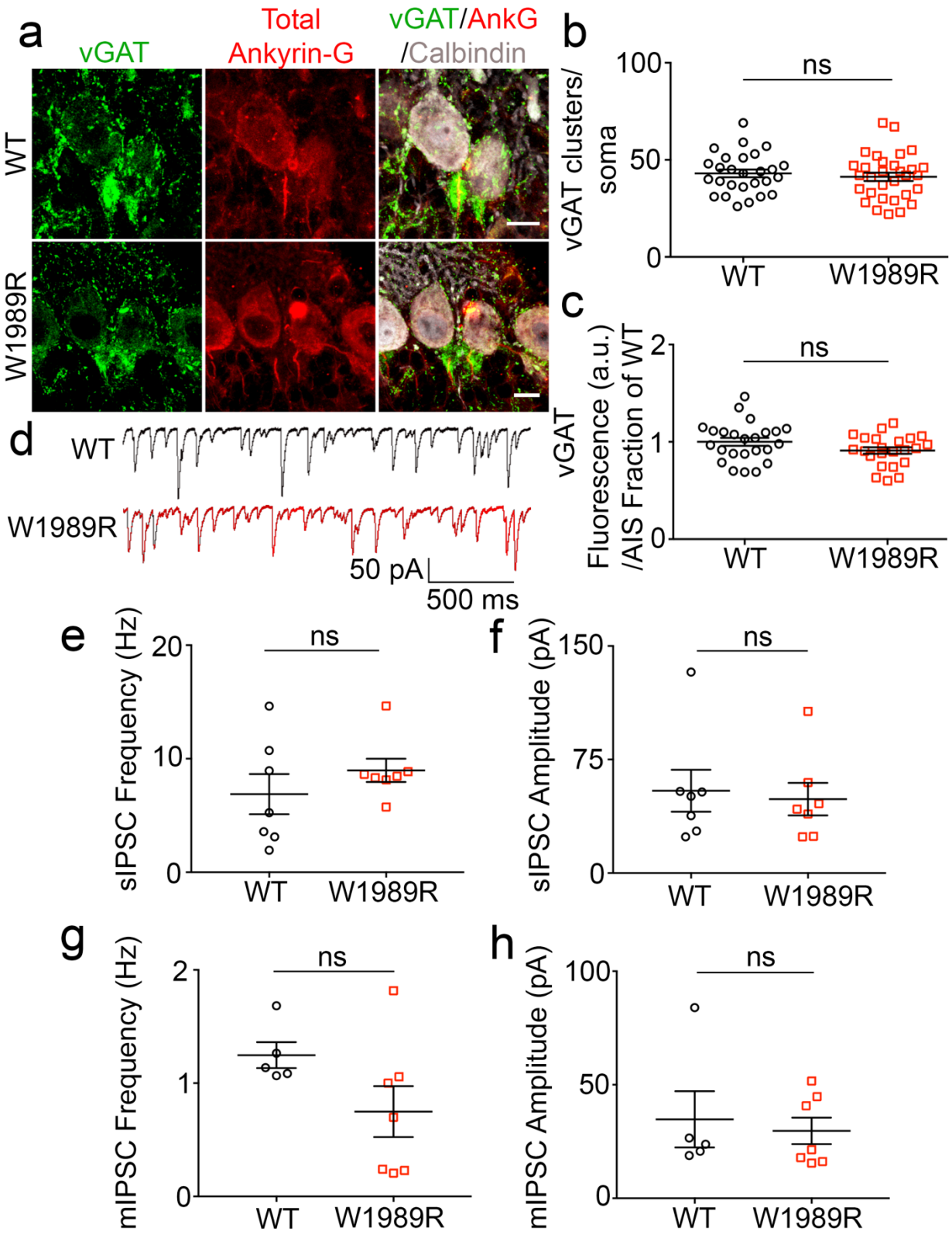
a
vGAT
Total
Ankyrin-G
vGAT/AnkG
/Calbindin
WT
W1989R
b
vGAT clusters/
soma
100
50
0
ns
WT
W1989R
c
vGAT
Fluorescence (a.u.)
/AIS Fraction of WT
2
1
0
ns
WT
W1989R
d
WT
W1989R
50 pA
500 ms
e
sIPSC Frequency (Hz)
20
10
0
ns
WT
W1989R
f
sIPSC Amplitude (pA)
150
75
0
ns
WT
W1989R
g
mIPSC Frequency (Hz)
2
1
0
ns
WT
W1989R
h
mIPSC Amplitude (pA)
100
50
0
ns
WT
W1989R

Supplementary Fig. 5: GABAergic synapses are maintained in the cerebellum of *Ank3* W1989R mice.

(a) Representative images of GABAergic synapses from cerebellar Purkinje neurons of P30 WT (top) and *Ank3* W1989R homozygous (bottom) mice. Sagittal brain sections immunostained for vGAT (green), total ankyrin-G (red), and calbindin (white). Scale bar: 10 µm. **(b)** Quantification of the total number of vGAT-positive clusters per soma above a set intensity threshold from WT (black circles) and *Ank3* W1989R homozygous (red squares) mice. *t-test* P = 0.54 (WT: 43.1 ± 2.0, N=3, n=27; W1989R: 41.3 ± 2.1, N=3, n=31). **(c)** Quantification of vGAT fluorescence intensity (a.u.) as fraction to WT between WT (black circles) and *Ank3* W1989R homozygous (red squares) mice. *t-test* P = 0.1 (WT: 1 ± 0.04, N=3, n=24; W1989R: 0.91 ± 0.03, N=3, n=23). **(d)** Spontaneous inhibitory post-synaptic current (sIPSC) representative traces from cerebellar Purkinje neurons in WT (black) and *Ank3* W1989R (red) slices. Scale bars: 50 pA, 500 ms. **(e)** Quantification of sIPSC frequency in WT (black circles) and *Ank3* W1989R (red squares) brain slices. *t-test* P = 0.33 (WT: 6.9 ± 1.8 Hz, n=7; W1989R: 8.9 ± 1.0 Hz, n=7). **(f)** Quantification of sIPSC amplitude in WT (black circles) and *Ank3* W1989R (red squares) brain slices. *t-test* P = 0.76 (WT: 54.4 ± 13.9 pA, n=7; W1989R: 48.8 ± 10.7 pA, n=7). **(g)** Quantification of mIPSC frequency in WT (black circles) and *Ank3* W1989R (red squares) brain slices. *t-test* P = 0.11 (WT: 1.23 ± 0.1 Hz, n=5; W1989R: 0.75 ± 0.2 Hz, n=7). **(h)** Quantification of mIPSC amplitude in WT (black circles) and *Ank3* W1989R (red squares) brain slices. *t-test* P = 0.69 (WT: 34.8 ± 12.4 pA, n=5; W1989R: 29.7 ± 5.8 pA, n=7).

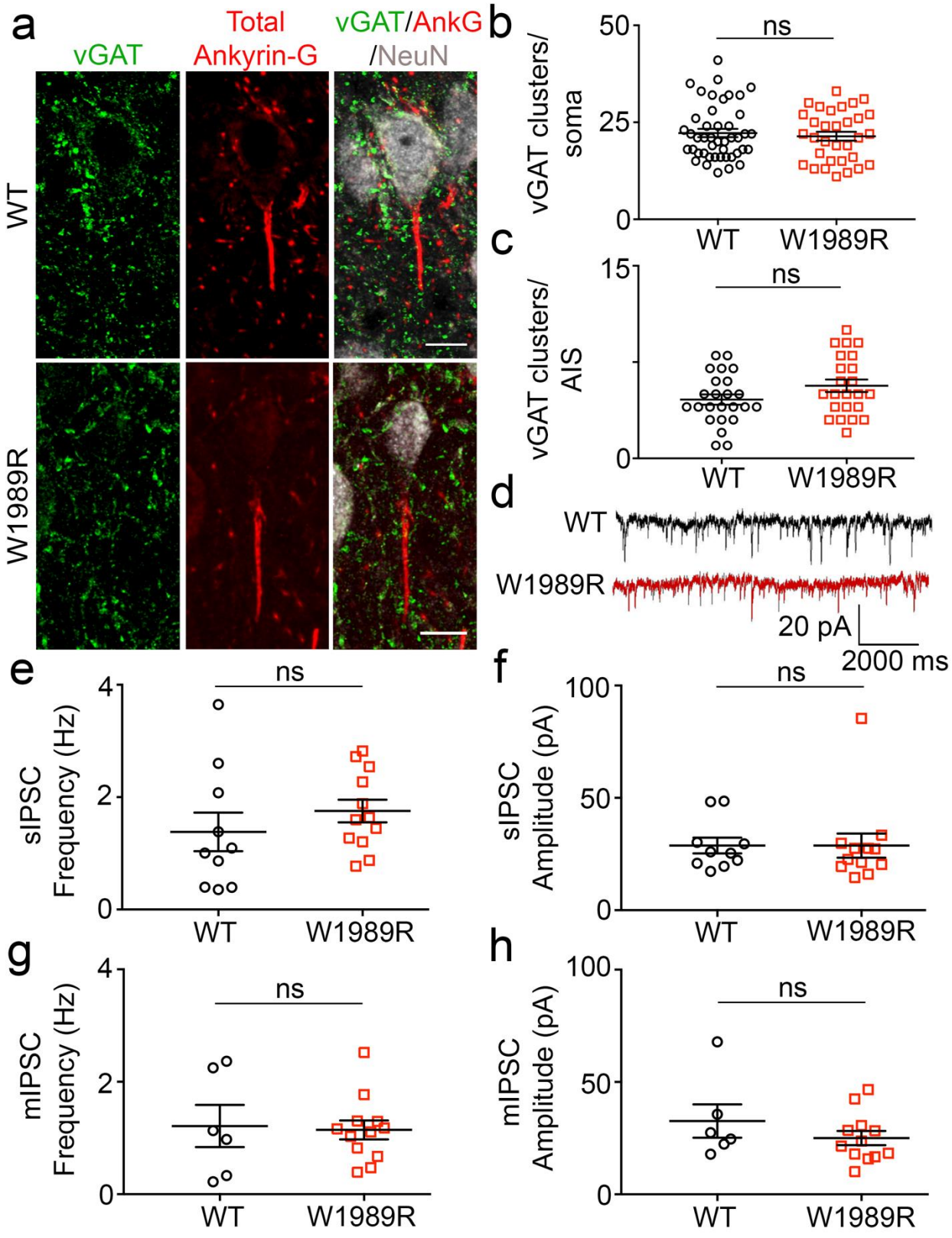
a
vGAT
Total Ankyrin-G
vGAT/AnkG /NeuN
WT
W1989R
b
vGAT clusters/ soma
50
25
0
ns
WT
W1989R
c
vGAT clusters/ AIS
15
0
ns
WT
W1989R
d
WT
W1989R
20 pA
2000 ms
e
sIPSC Frequency (Hz)
4
2
0
ns
WT
W1989R
f
sIPSC Amplitude (pA)
100
50
0
ns
WT
W1989R
g
mIPSC Frequency (Hz)
4
2
0
ns
WT
W1989R
h
mIPSC Amplitude (pA)
100
50
0
ns
WT
W1989R

Supplementary Fig. 6: Thalamic neurons display normal inhibitory currents in *Ank3* W1989R mice.

(a) Representative images of GABAergic synapses on thalamic neurons of P30 WT (top) and *Ank3* W1989R homozygous (bottom) mice. Coronal brain sections immunostained for vGAT (green), total ankyrin-G (red), and NeuN (white). Scale bar: 10 µm. **(b)** Quantification of the total number of vGAT-positive clusters per soma above a set intensity threshold from WT (black circles) and *Ank3* W1989R homozygous (red squares) mice. *t-test* P = 0.6 (WT: 22.2 ± 1.1, N=3, n=45; W1989R: 21.4 ± 1.2, N=3, n=32. **(c)** Quantification of total number of vGAT-positive clusters per AIS from WT (black circles) and *Ank3* W1989R homozygous (red squares) mice. *t-test* P = 0.09 (WT: 4.6 ± 0.4, N=3, n=24; W1989R: 5.7 ± 0.5, N=3, n=23). **(d)** Spontaneous inhibitory post-synaptic current (sIPSC) representative traces from thalamic neurons in WT (black) and *Ank3* W1989R (red) slices. Scale bars: 20 pA, 2000 ms. **(e)** Quantification of sIPSC frequency in WT (black circles) and *Ank3* W1989R (red squares) brain slices. *t-test* P = 0.34 (WT: 1.4 ± 0.3 Hz, n=10; W1989R: 1.8 ± 0.2 Hz, n=12). **(f)** Quantification of sIPSC amplitude in WT (black circles) and *Ank3* W1989R (red squares) brain slices. *t-test* P = 0.99 (WT: 28.8 ± 3.5 pA, n=10; W1989R: 28.8 ± 5.4 pA, n=12). **(g)** Quantification of mIPSC frequency in WT (black circles) and *Ank3* W1989R (red squares) brain slices. *t-test* P = 0.84 (WT: 1.2 ± 4 Hz, n=6; W1989R: 1.1 ± 0.2 Hz, n=12). **(h)** Quantification of mIPSC amplitude in WT (black circles) and *Ank3* W1989R (red squares) brain slices. *t-test* P = 0.28 (WT: 32.6 ± 7.4 pA, n=6; W1989R: 25.0 ± 3.2 pA, n=12).

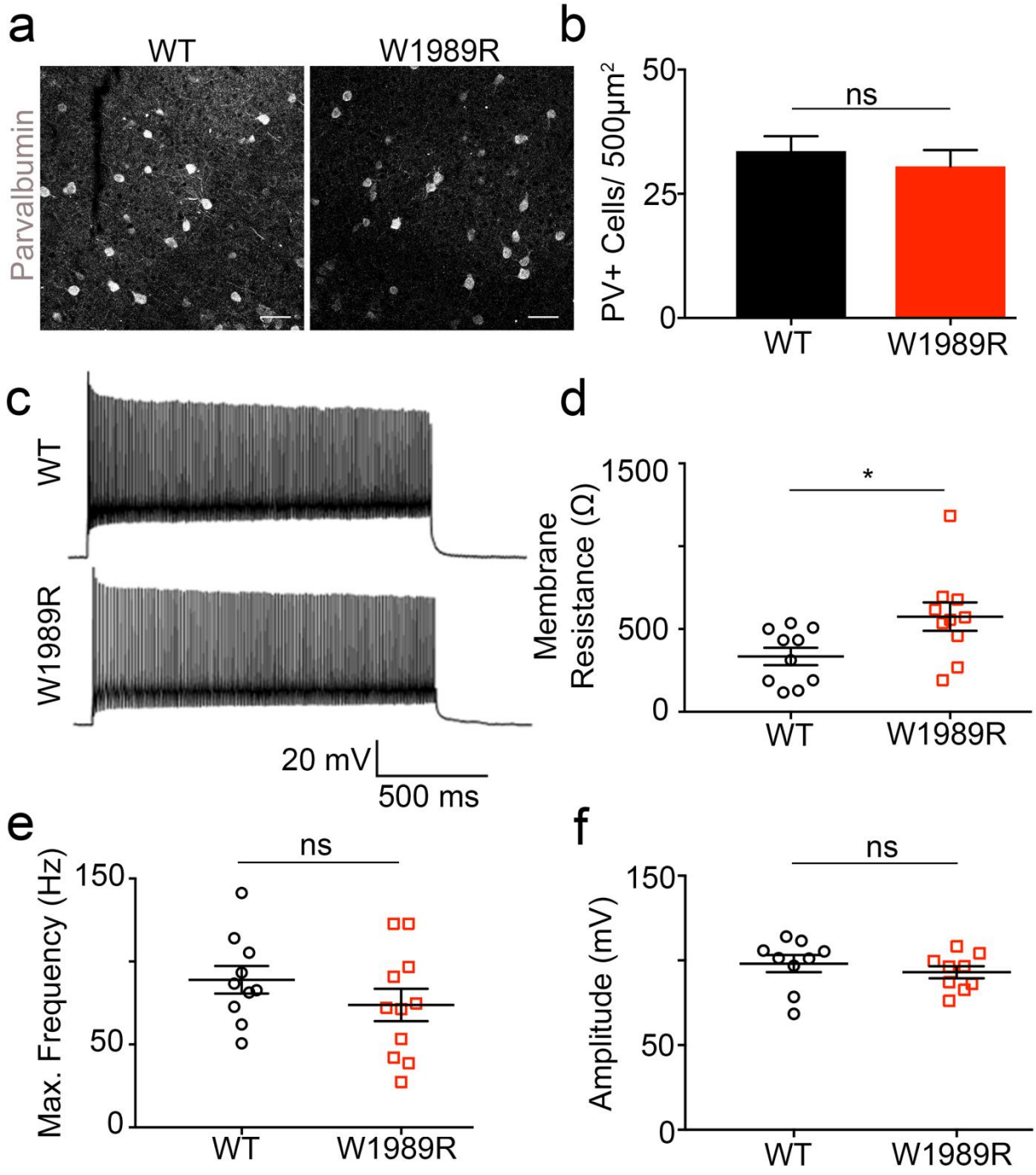
a
WT
W1989R
Parvalbumin
b
PV+ Cells/ 500µm²
50
25
0
ns
WT
W1989R
c
WT
W1989R
20 mV
500 ms
d
Membrane Resistance (Ω)
1500
500
0
*
WT
W1989R
e
Max. Frequency (Hz)
150
50
0
ns
WT
W1989R
f
Amplitude (mV)
150
50
0
ns
WT
W1989R

Supplementary Fig. 7*:* Normal density and fast-spiking properties of *Ank3* W1989R PV+ GABAergic interneurons.

(a) Representative images of parvalbumin-positive (PV+) interneurons in layer II/III somatosensory cortex of P30 WT (left) and *Ank3* W1989R homozygous (right) mice. Coronal brain sections immunostained with PV (white). Scale bar: 50 µm. **(b)** Quantification of total number of PV-positive cells per 500 μm^2 from WT (black bar) and *Ank3* W1989R homozygous (red bar) sections. *t-test* P = 0.497, ns, not significant (WT: 33.6 ± 3.0, N=3, n=15; W1989R: 30.5 ± 3.3, N=3, n=14). **(c)** Representative traces of evoked firing patterns and AP frequencies of fast-spiking PV+ interneurons in layer II/III somatosensory cortex from WT (top) and *Ank3* W1989R homozygous (bottom) brain slices. Scale bar: 20 mV, 500 ms. **(d)** Quantification of membrane resistance of PV+ cells in WT (black circles) and *Ank3* W1989R homozygous (red squares). *t-test* *P = 0.0276 (WT: 334.5 ± 52.8, n=10; W1989R: 574.9 ± 85.31, n=10). **(e)** Quantification of PV+ cell maximum frequency in WT (black circles) and *Ank3* W1989R homozygous (red squares). *t-test* P = 0.256 (WT: 89.0 ± 8.3, n=10; W1989R: 73.8 ± 9.7, n=11). **(f)** Quantification of single AP amplitude of PV+ in WT (black circles) and *Ank3* W1989R homozygous (red squares). *t-test* P = 0.422 (WT: 98.1 ± 5.0, n=9; W1989R: 93.0 ± 3.5, n=10). Data shown as mean ± SEM.

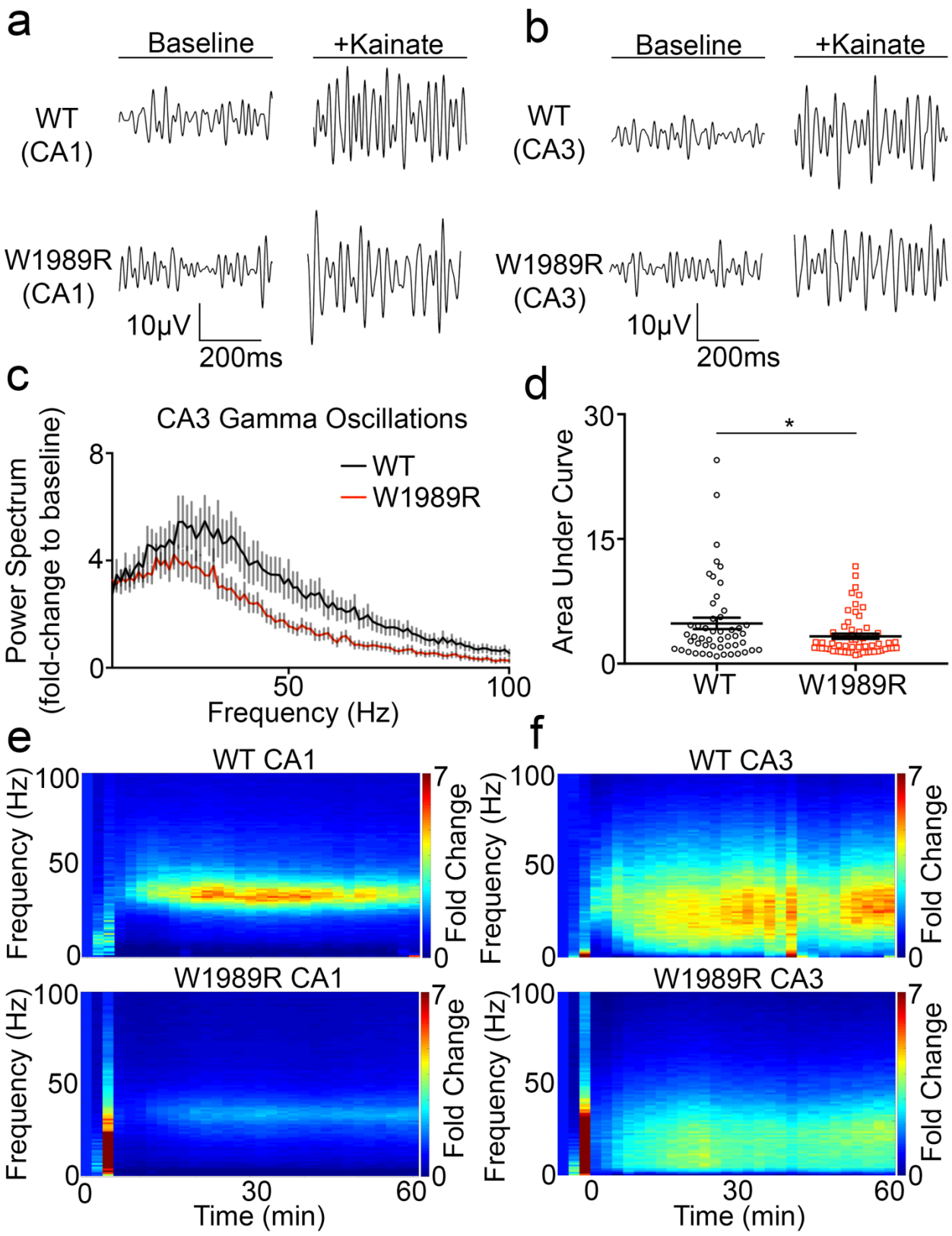
a
Baseline
+Kainate
WT
(CA1)
W1989R
(CA1)
10μV
200ms
b
Baseline
+Kainate
WT
(CA3)
W1989R
(CA3)
10μV
200ms
c
CA3 Gamma Oscillations
WT
W1989R
Power Spectrum
(fold-change to baseline)
Frequency (Hz)
d
Area Under Curve
*
WT
W1989R
e
WT CA1
W1989R CA1
Frequency (Hz)
Fold Change
Time (min)
f
WT CA3
W1989R CA3
Frequency (Hz)
Fold Change
Time (min)

Supplementary Fig. 8: Reduced gamma oscillations in the hippocampus of *Ank3* W1989R mice.

(a) Representative traces of kainate-induced gamma oscillations from local field potential (LFP) recordings in CA1 hippocampal neurons and **(b)** CA3 hippocampal neurons of WT (top) or *Ank3* W1989R homozygous (bottom) mice in acute brain slices. **(c)** Power spectral analysis from CA3 hippocampus WT (black circles) and *Ank3* W1989R homozygous (red squares) mice. **(d)** Quantification of the area under the curve for gamma band (30-60Hz) from WT (black circles) and *Ank3* W1989R homozygous (red squares). *t-test* *P=0.0343 (WT: 4.85 ± 0.7, N=5, n=50; W1989R: 3.3 ± 0.3, N=5, n=59). **(e)** Representative time-frequency sonograms of CA1 hippocampal neurons from WT (top) and W1989R homozygous (bottom) mice. **(f)** Representative time-frequency sonograms of CA3 hippocampal neurons from WT (top) and W1989R homozygous (bottom) mice.

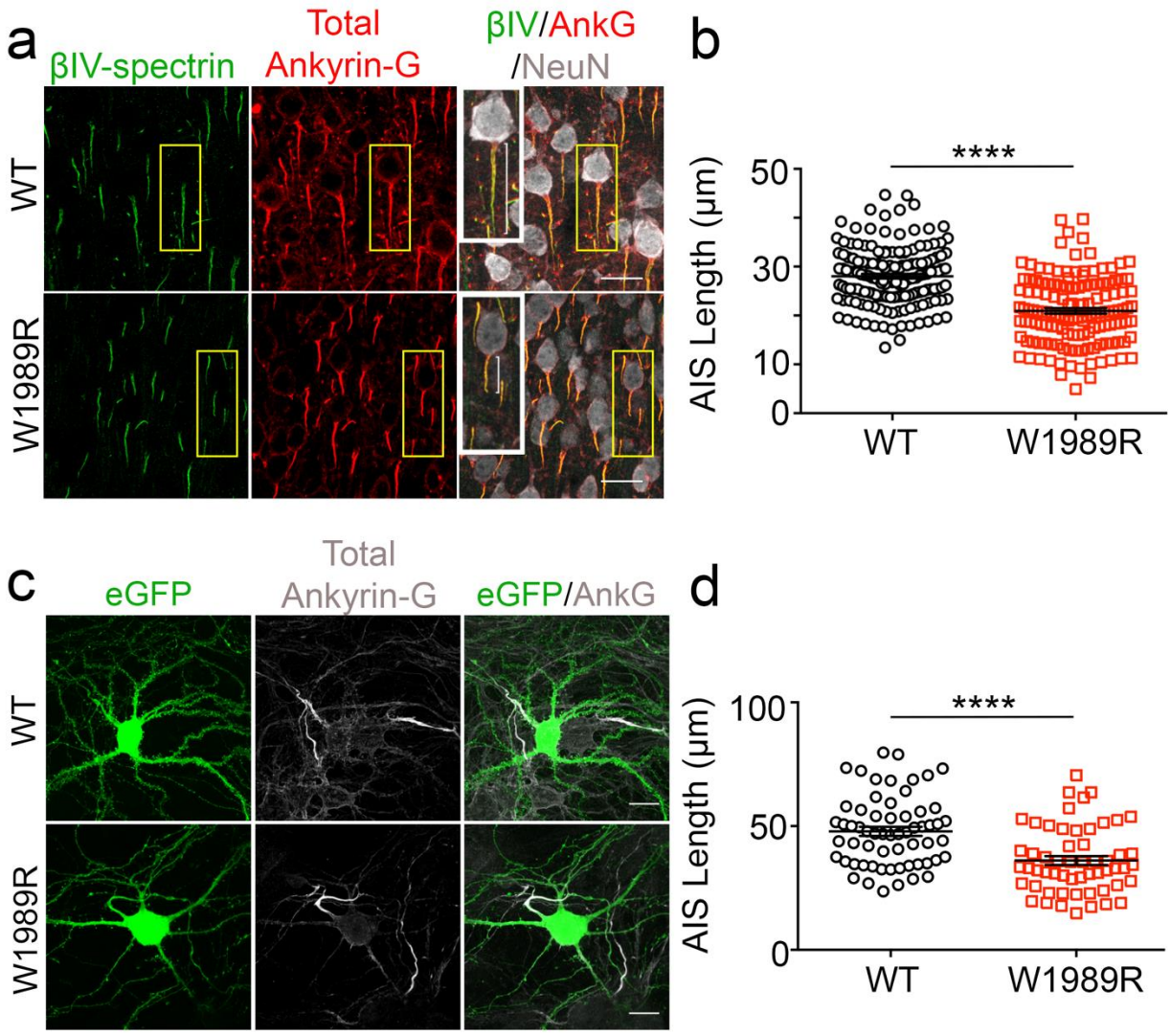
a
βIV-spectrin
Total
Ankyrin-G
βIV/AnkG
/NeuN
WT
W1989R
b
AIS Length (μm)
50
30
10
0
****
WT
W1989R
c
eGFP
Total
Ankyrin-G
eGFP/AnkG
WT
W1989R
d
AIS Length (μm)
100
50
0
****
WT
W1989R

Supplementary Fig. 9: Cortical and hippocampal pyramidal neurons have decreased AIS length in *Ank3* W1989R mice.

(a) Representative images from coronal sections of layer II/III somatosensory cortex of P30 WT (top) and *Ank3* W1989R homozygous (bottom) mice. Immunostaining for βIV-spectrin (green), total ankyrin-G (red), and NeuN (white). Scale bar: 20 µm. **(b)** Quantification of AIS length between WT (black circles) and W1989R homozygous (red squares) mice. *t-test* ****P < 0.0001 (WT: 28.03 ± 0.5, N=3, n=156; W1989R: 20.94 ± 0.6, N=3, n=140). **(c)** Representative images of dissociated hippocampal cultured neurons from WT (left) and *Ank3* W1989R homozygous (right) mice at 21DIV filled with soluble eGFP. Scale bar: 20 µm. **(d)** Quantification of the AIS length between WT (black circles) and *Ank3* W1989R homozygous (red squares) neurons. *t-test* ****P < 0.0001 (WT: 47.87 ± 1.8, N=3, n=61; W1989R: 36.11 ± 1.8, N=3, n=56).

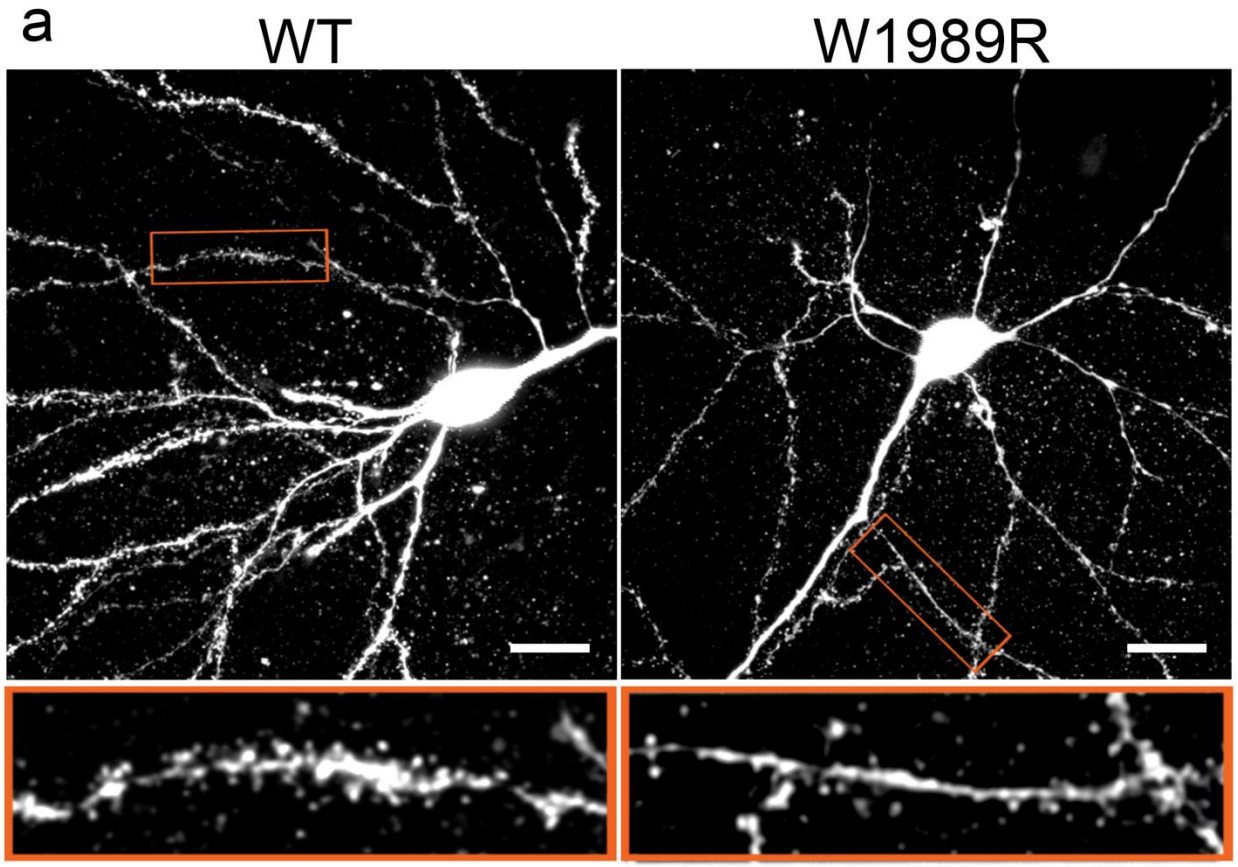
a
WT
W1989R

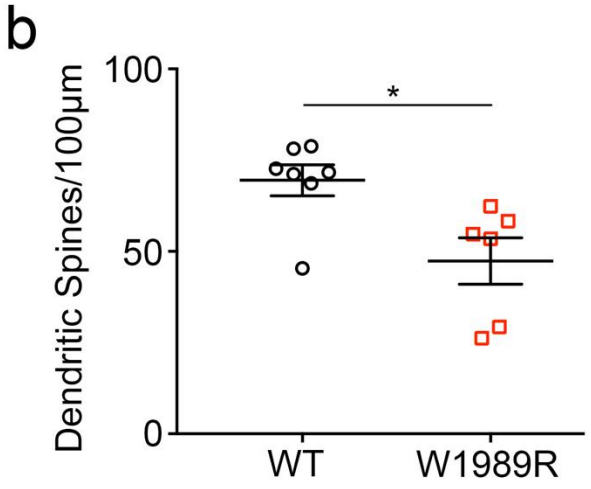
b
Dendritic Spines/100μm
100
50
0
*
WT
W1989R

Supplementary Fig. 10: Decreased dendritic spine density in CA1 hippocampal pyramidal neurons in *Ank3* W1989R mice *in vivo*.

(a) Representative images of biocytin-filled CA1 hippocampal pyramidal neurons of P30 WT (left) and *Ank3* W1989R homozygous (right) mice. Images were pseudocolored white. Scale bar: 20 µm. **(b)** Quantification of the number of dendritic spines per 100 µm of dendrite length in CA1 hippocampal pyramidal neurons. *t-test* *P < 0.01 (WT: 69.5 ± 4.3, N=3, n=7; W1989R: 47.4 ± 6.3, N=3, n=6).

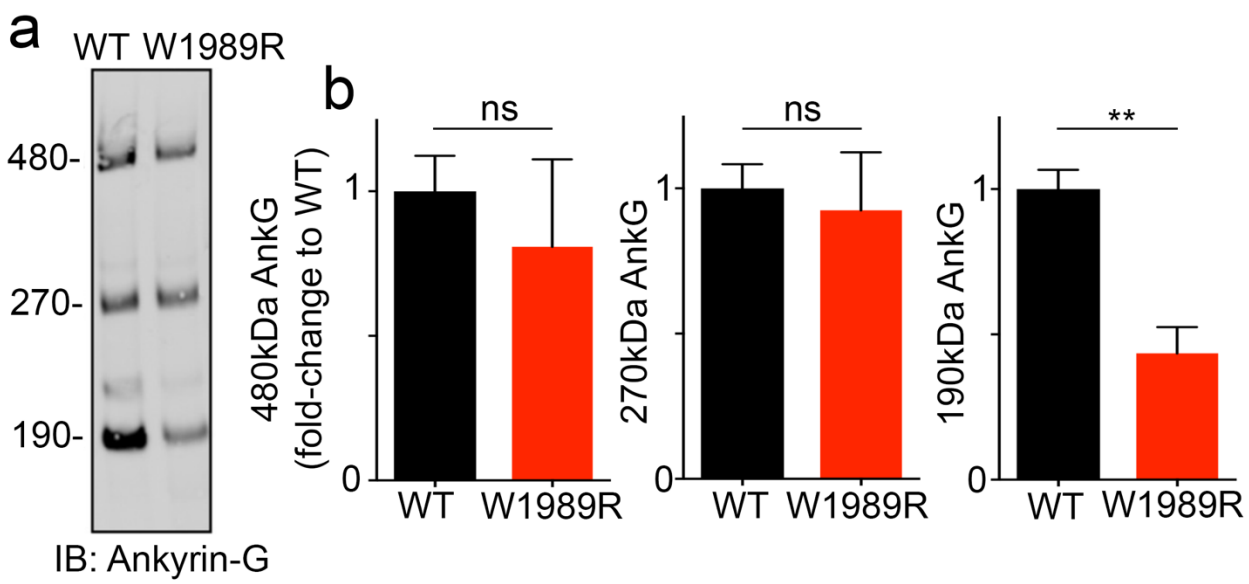

Supplementary Fig. 11: 190 kDa ankyrin-G expression levels are reduced in cortex of *Ank3* W1989R mice.

(a) Western blot analysis from cortical lysates of P30 WT (left) and *Ank3* W1989R homozygous (right) mice. Blots were probed with antibodies to total ankyrin-G. **(b)** Quantification of relative expression levels of 480 kDa ankyrin-G *t-test* P = 0.59 (WT: 1.0 ± 0.1, N=3; W1989R: 0.81 ± 0.3, N=3), 270 kDa ankyrin-G *t-test* P = 0.75 (WT: 1.0 ± 0.1, N=3; W1989R: 0.92 ± 0.2, N=3), and 190 kDa ankyrin-G *t-test* **P = 0.0073 (WT: 1 ± 0.1 N=3; W1989R: 0.43 ± 0.1, N=3). Data normalized to WT controls. Data shown as mean ± SEM.

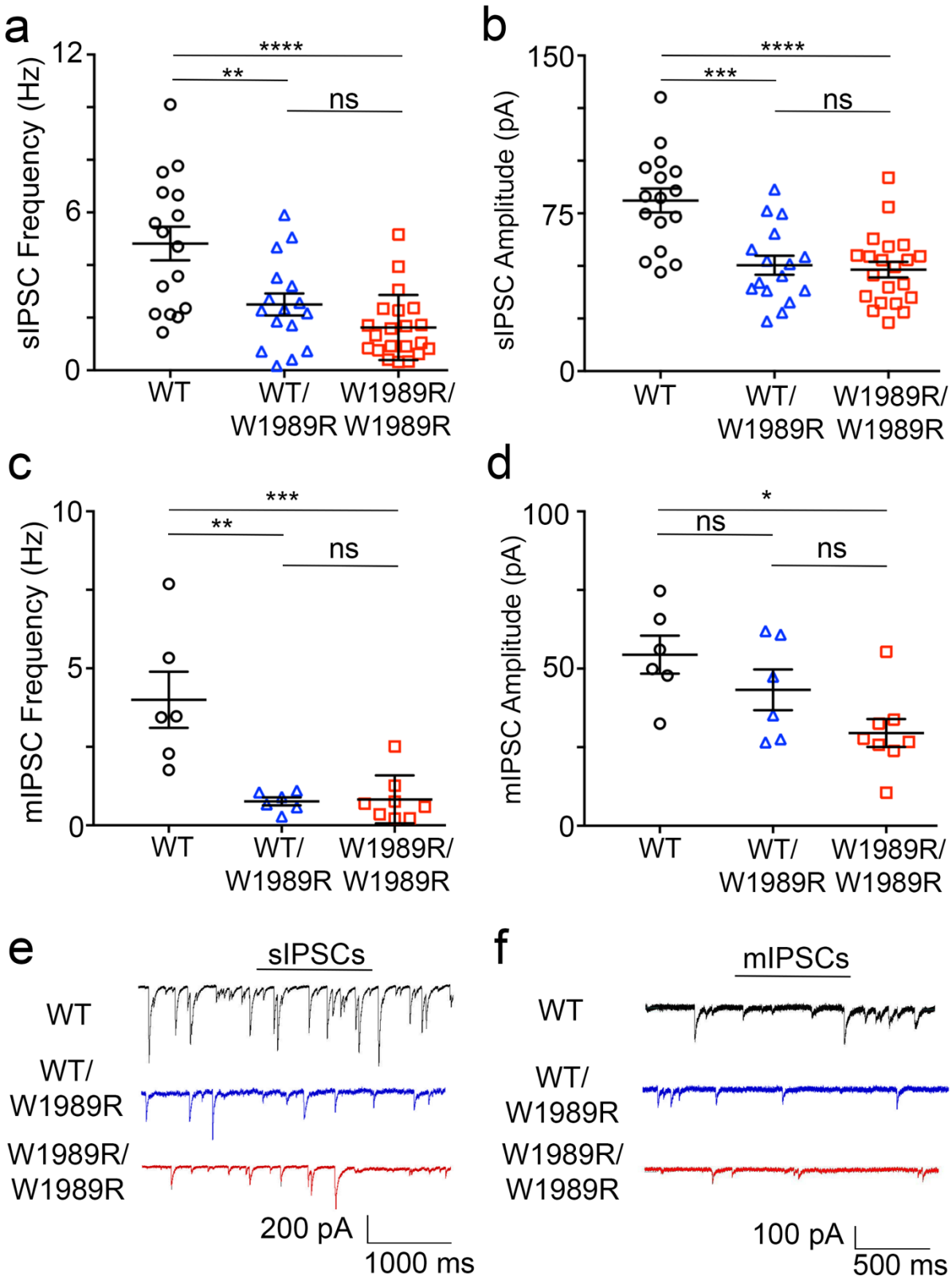
a
sIPSC Frequency (Hz)
12
6
0
****
**
ns
WT
WT/ W1989R
W1989R/ W1989R
b
sIPSC Amplitude (pA)
150
75
0
****
***
ns
WT
WT/ W1989R
W1989R/ W1989R
c
mIPSC Frequency (Hz)
10
5
0
***
**
ns
WT
WT/ W1989R
W1989R/ W1989R
d
mIPSC Amplitude (pA)
100
50
0
*
ns
ns
WT
WT/ W1989R
W1989R/ W1989R
e
sIPSCs
WT
WT/ W1989R
W1989R/ W1989R
200 pA
1000 ms
f
mIPSCs
WT
WT/ W1989R
W1989R/ W1989R
100 pA
500 ms

Supplementary Fig. 12: Heterozygous *Ank3* W1989R mice have reduced GABAergic synapse function.

Comparison of P25-48 heterozygous *Ank3* W1989R mice to wild-type and homozygous *Ank3* W1989R mice. Note: wild-type and *Ank3* W1989R homozygous mouse data are from Fig. 2 and Supplemental Fig. 4 and shown for comparison purposes. **(a)** Quantification of sIPSC frequency in WT (black circles), heterozygous *Ank3* WT/W1989R (blue triangles), and homozygous *Ank3* W1989R/W1989R (red squares) brain slices. *One-way ANOVA, Tukey's post hoc.* WT vs. WT/W1989R **P = 0.0023, WT vs. W1989R/W1989R ****P < 0.0001, WT/W1989R vs. W1989R/W1989R P = 0.33 (WT: n=16; WT/W1989R: n=16; W1989R/W1989R n=21). **(b)** Quantification of sIPSC amplitude in WT (black circles), heterozygous *Ank3* WT/W1989R (blue triangles), and homozygous *Ank3* W1989R/W1989R (red squares) slices. *One-way ANOVA, Tukey's post hoc.* WT vs. WT/W1989R ***P = 0.0001, WT vs. W1989R/W1989R ****P < 0.0001, WT/W1989R vs. W1989R/W1989R P = 0.94 (WT: n=16; WT/W1989R: n=16; W1989R/W1989R n=21). **(c)** Quantification of mIPSC frequency in WT (black circles), heterozygous *Ank3* WT/W1989R (blue triangles), and homozygous *Ank3* W1989R/W1989R (red squares) slices. *One-way ANOVA, Tukey's post hoc.* WT vs. WT/W1989R **P = 0.001, WT vs. W1989R/W1989R ***P = 0.0008, WT/W1989R vs. W1989R/W1989R P = 0.99 (WT: n=6; WT/W1989R: n=6; W1989R/W1989R n=8). **(d)** Quantification of mIPSC amplitude in WT (black circles), heterozygous *Ank3* WT/W1989R (blue triangles), and homozygous *Ank3* W1989R/W1989R (red squares) slices. *One-way ANOVA, Tukey's post hoc.* WT vs. WT/W1989R P = 0.38, WT vs. W1989R/W1989R *P = 0.01, WT/W1989R vs. W1989R/W1989R P = 0.21 (WT: n=6;

WT/W1989R: n=6; W1989R/W1989R n=8). **(e)** Representative traces of spontaneous inhibitory post-synaptic currents (sIPSCs) of layer II/III somatosensory cortical neurons in WT (black circles), heterozygous *Ank3* WT/W1989R (blue triangles), and homozygous *Ank3* W1989R/W1989R (red squares) slices. Scale bars: 200 pA, 1000 ms. **(f)** Representative traces of miniature inhibitory post-synaptic currents (mIPSCs) from layer II/III somatosensory cortical neurons in WT (black), and *Ank3* W1989R (red) homozygous brain slices. Scale bar: 100 pA, 500 ms.

Table 1: Statistics of X-ray Crystallographic Data Collection and Model Refinement

Data Collection:

Data sets	Ankyrin-G/ GABARAP
Space group	I23
Wave length (Å)	0.9785
Unit Cell Parameters	a=b=c=96.99 a=b=γ=90°
Resolution range (Å)	50-2.20 *2.24-2.20)
No. of unique reflections	7843 (367)
Redundancy	20.0 (19.6)
I/σ	45.2 (2.6)
Completeness (%)	99.9 (100)
R_{merge} [a] (%)	6.9 (>100)
$CC_{1/2}$ (last resolution shell)[b]	0.792
Structure refinement:	
Resolution (Å)	50-2.20 (2.77-2.20)
R_{crvst} [c]/R_{free} [d] (%)	20.27/24.89 (25.57/30.84)
rmsd bonds (Å) / angles (°)	0.006 / 0.93
Average B factor (Å^2) [e]	34.2
No. of atoms	
Protein atoms	1087
Water	15
No. of reflections	
Working set	7396 (3611)
Test set	349 (174)
Ramachandran plot regions	
Favored (%)	98.5
Allowed (%)	1.5
Outliers (%)	0

Table 1: Statistics of x-ray crystallographic data collection and model refinement.

Summary statistics of X-ray crystallography data from the crystal structures in Fig. 1 and Supplemental Fig. 1.

Table 2: Cell-Type Electrophysiological Properties between WT and *Ank3* W1989R mice

		Membrane Resistance (MΩ)	Membrane Potential (mV)	AP Threshold (mV)	AP Amplitude (mV)	AP Peak Time (ms)	AP Width (ms)	AP Tau (ms)
Pyramidal	WT	228.3 ± 121 (n=27)	-67.5 ± 4 (n=22)	-40.7 ± 20 (n=22)	113.7 ± 13 (n=22)	2.6 ± 0.5 (n=22)	2.6 ± 0.6 (n=22)	25 ± 10 (n=22)
	W1989R	159.9 ± 66* (n=33)	-66.3 ± 5 (n=29)	-36.1 ± 30 (n=29)	111 ± 14 (n=29)	2.7 ± 1 (n=29)	2.8 ± 1 (n=29)	21.6 ± 10 (n=25)
Fast-Spiking	WT	334.6 ± 167 (n=10)	-62.1 ± 5 (n=9)	-46.3 ± 2 (n=9)	98.1 ± 15 (n=9)	2.1 ± 0.4 (n=9)	0.8 ± 0.1 (n=9)	0.9 ± 0.3 (n=9)
	W1989R	574.3 ± 269* (n=9)	-61.6 ± 6 (n=9)	-46.3 ± 2 (n=9)	93 ± 11 (n=9)	2.2 ± 0.4 (n=9)	1.0 ± 0.4 (n=9)	1.2 ± 0.8 (n=9)
Regular Spiking Nonpyramidal	WT	363.9 ± 108 (n=13)	-64.8 ± 5 (n=13)	-41 ± 10 (n=9)	110.2 ± 9 (n=9)	2.4 ± 0.2 (n=13)	2.5 ± 0.7 (n=13)	17.5 ± 11 (n=13)
	W1989R	284.3 ± 125 (n=17)	-57.5 ± 28 (n=18)	-47 ± 6* (n=18)	101.4 ± 15 (n=18)	2.6 ± 0.9 (n=18)	2.4 ± 0.2 (n=18)	12.4 ± 11 (n=17)
Irregular Spiking	WT	227.03 (n=1)	-60.9 ± 5 (n=3)	-43.9 ± 2 (n=3)	88.3 ± 5.6 (n=3)	3.1 ± 0.4 (n=3)	3.0 ± 0.5 (n=3)	9.5 ± 0.7 (n=3)
	W1989R	156.2 ± 14 (n=4)	-64.2 ± 4 (n=4)	-49.4 ± 1* (n=4)	107.4 ± 12 (n=4)	2.7 ± 0.2 (n=4)	3.1 ± 0.3 (n=4)	9.1 ± 1 (n=4)

Table 2: Comparison of cell-type specific electrophysiological properties between WT and *Ank3* W1989R mice. Quantification of various electrophysiology measurements of layer II/III cortical pyramidal neurons and the main classes of inhibitory interneurons following evoked APs in acute brain slices from WT and *Ank3* W1989R homozygous mice. Yellow/asterisk indicates significantly different from WT.

Table 3: Cell-type specific morphological and functional changes in *Ank3* W1989R mice

	vGAT (+) GABAergic Synapses	Inhibitory Post-synaptic Currents	Action Potential Firing Rate	Dendritic Spine Density	AIS Length
Layer II/III Somatosensory Cortical Pyramidal Neurons	↓	↓	↑	N.D.	↓
CA1 Hippocampal Pyramidal Neurons	↓	↓	↑	↓	↓
Thalamic Neurons	—	—	N.D.	N.D.	—
Cerebellar Purkinje Neurons	—	—	N.D.	N.D.	—

Table 3: Summary of cell-type specific morphological and functional differences in *Ank3* W1989R mice compared to WT. Summary of results demonstrating differences in GABAergic synapse number, GABA-mediated currents, action potential firing rate, dendritic spine density, and AIS length of layer II/III cortical and hippocampal pyramidal neurons, thalamic neurons, and cerebellar Purkinje neurons in *Ank3* W1989R mice compared to WT mice. Blue arrows indicate significantly decreased from WT, red arrows indicate significantly increased from WT, black lines indicate no difference from WT. N.D. represents not determined.